Brittle Failure in Compression: Splitting, Faulting and Brittle-Ductile Transition

H. Horii and S. Nemat-Nasser

Phil. Trans. R. Soc. Lond. A 1986 **319**, 337-374
doi: 10.1098/rsta.1986.0101

Phil. Trans. R. Soc. Lond. A **319**, 337–374 (1986)

Printed in Great Britain

BRITTLE FAILURE IN COMPRESSION: SPLITTING, FAULTING AND BRITTLE–DUCTILE TRANSITION

By H. HORII† and S. NEMAT-NASSER‡

Department of Civil Engineering, The Technological Institute, Northwestern University, Evanston, Illinois 60201, *U.S.A.*

(*Communicated by M. F. Ashby, F.R.S. – Received* 30 *April* 1985)

[Plates 1–6]

CONTENTS

---

† Present address: Department of Civil Engineering, University of Tokyo, Bunkyo-ku, Tokyo 113, Japan.

‡ Present address: Department of Applied Mechanics and Engineering Sciences, University of California, San Diego, La Jolla, California 92093, U.S.A.

Vol. 319. A. 1549 [Published 16 September 1986

The micromechanics of brittle failure in compression and the transition from brittle to ductile failure, observed under increasing confining pressures, are examined in the light of existing experimental results and model studies. First, the micromechanics of axial splitting and faulting is briefly reviewed, certain mathematical models recently developed for analysing these failure modes are outlined, and some new, simple closed-form analytic solutions of crack growth in compression and some new quantitative model experimental results are presented. Then, a simple two-dimensional mathematical model is proposed for the analysis of the brittle–ductile transition process, the corresponding elasticity boundary-value problem is formulated in terms of singular integral equations, the solution method is given, and numerical results are obtained and their physical implications are discussed. In addition, a simple closed-form analytic solution is presented and, by comparing its results with those of the exact formulation, it is shown that the analytic estimates are reasonably accurate in the range of the brittle response of the material. Finally, the results of some laboratory model experiments are reported in an effort to support the mathematical models.

1. Introduction

The overall mechanical response of brittle solids, such as rock and concrete, is known to be greatly influenced by temperature, pressure, and strain rate; the pore fluid pressure, if present, is also important, but in this paper we consider the behaviour of 'dry' samples. At suitably high temperatures and low strain rates, the inelastic deformation of materials of this kind is rate-dependent, stemming from diffusion, nonlinear creep, and even recrystallization. Below a certain temperature and above a certain strain rate, the overall inelasticity is caused by essentially rate-independent slip and twinning in single crystal constituents, or by microfracturing and faulting, depending on the magnitude of the overall confining pressure (see, for example, Ashby & Verrall (1977), Tullis & Yund (1977), Paterson (1978), Tullis (1979) and Kirby & Kronenberg (1984)).

In this paper, attention is focused on the inelastic deformations associated with low temperature, essentially rate-independent processes that lead to the following failure modes, depending on the magnitude of the confining pressure: (1) axial splitting of the sample by macroscopic cracks extending in the direction of axial compression, in the absence of any lateral confining pressure; (2) faulting or *macroscopic* shear failure, when axial compression is accompanied by moderate confining pressure; and finally, (3) ductile flow in the presence of a suitably large confining pressure (see, for example, Griggs & Handin (1960), Fairhurst & Cook (1966), Mogi (1966), Holzhausen (1978), Holzhausen & Johnson (1979), Paterson (1978) and Kranz (1983), who review the literature and give an extensive list of references). The overall axial-stress–axial-strain curve associated with low confinement includes a peak stress followed by a sharp descending portion. The resistance to further straining beyond the peak stress increases with increasing confining pressure, and eventually there emerges a stress–strain curve akin to ductile metals, with a knee and a work-hardening portion. Furthermore, the fault zone which is a sharply defined failure plane at low pressures, broadens to a zone of intense deformation with increasing pressure. With further increase in the confining pressure, a transition from brittle to ductile response gradually takes place as the macroscopic deformation of the sample becomes more uniformly distributed throughout the sample (see, for example, Donath *et al.* (1971)). An increase in temperature has an important role in promoting ductility. The confining pressure associated with the brittle–ductile transition decreases with increasing temperature.

For the temperature range considered here, where rate effects may be ignored, microcracking and plastic flow of the crystalline constituents are the two major, often competing, sources of the overall inelastic response of rocks and other similar brittle materials. Microscopic observations have shown that cracks may nucleate under axial compression at various microscopic inhomogeneities, such as grain boundary cavities, the interface between dissimilar constituents, the intersection of slip bands with an adjacent grain, and other possible material or geometric discontinuities (see, for example, Sprunt & Brace (1974), Olsson & Peng (1976), Tapponnier & Brace (1976), Wong (1982) and Kranz (1983)). With a relatively low confining pressure, there emerges a narrow region of high crack density, which eventually becomes a fault plane at the axial stress close to the ultimate strength (see Scholz (1968), Hoshino & Koide (1970), Hallbauer *et al.* (1973), Olsson & Peng (1976), Lockner & Byerlee (1977) and Wong (1982)). At high values, on the other hand, the confining pressure suppresses this process, leading instead to either cataclastic flow characterized by distributed microcracking, or to ductile flow produced by plastic deformation throughout the sample, depending on the material and the temperature and pressure levels. In granite, for example, Tullis & Yund (1977) report throughgoing faults observed at low temperatures in axially compressed samples under less than 500 MPa (5 kbar) pressure, and under 750–1500 MPa (7.5–15 kbar) pressure there is cataclastic deformation consisting of grain-size faults without any macroscopic faulting, up to 15–20 % axial shortening. A transition from dominantly microcracking to dominantly dislocation motion is reported by these authors at approximately 300–400 °C for quartz and 550–650 °C for feldspar. For pyroxenes, on the other hand, Kirby & Kronenberg (1984) report that, at suitably high pressures, ductile flow by low-temperature plastic flow can be induced even at room temperature. Similar results are reported for marble and limestone, where cataclastic microcracking can be essentially suppressed at ordinary temperatures with high enough confining pressures (see Donath *et al.* (1971) and Tobin & Donath (1971)).

Based on microscopic observations, various mathematical models have been introduced in an effort to analyse the failure process of brittle materials in compression. Most of these models are grounded in the idea that frictional sliding of a pre-existing crack produces, at the crack tips, tension cracks that grow in the direction of maximum compression (see McClintock & Walsh (1963), Kachanov (1982), Ashby & Cookley (1986) and Steif (1984)). In addition, model experiments on glass and photoelastic plates containing pre-existing cracks or slits have been performed to illustrate the process of out-of-plane crack growth in compression (Brace & Bombolakis 1963; Hoek & Bieniawski 1965). In particular, Nemat-Nasser & Horii (1982) and Horii & Nemat-Nasser (1985*a*) have examined the consequences of a straight flaw model endowed with frictional resistance and cohesion, by formulating and solving the associated two-dimensional elasticity problem and by comparing the results with the corresponding model experiments. These authors show analytically and verify experimentally that, under axial compression, tension cracks nucleate from the tips of the flaw at an angle close to 70° with respect to the flaw orientation, and grow with increasing axial load, curving toward the direction of the maximum axial compression. If the axial compression is accompanied by any amount of lateral tension, the crack growth becomes unstable after a certain crack length is attained, resulting in axial splitting. If, on the other hand, some lateral compression accompanies the axial load, the tension cracks grow to a certain length and then stop. To model faulting observed in the presence of a confining pressure, these authors consider a row of flaws and calculate the length of the tension cracks emanating from the tips of these flaws and growing under an increasing axial load. Depending on the overall orientation of the row of flaws, it turns out that such a crack growth process can also become unstable, leading to the formation of a fault. By considering a reasonable relation between flaw size and flaw spacing, Horii & Nemat-Nasser show that the model predicts the observed strength curves and fault orientations for sandstone and granite.

The main objective of the present paper is to examine the micromechanics of the transition, observed with increasing confining pressures, from brittle failure to ductile deformation. It is shown that, as the confining pressure increases, the unstable growth of tension cracks emanating from the tips of a row of flaws is suppressed, and with it the associated faulting. With increasing confining pressure, the contribution to inelastic deformation by microcracking decreases while that by plastic flow increases. Based on microscopic observation and results of our *model* experiments, a mathematical model for the brittle–ductile transition process is proposed. The model consists of an isolated thin straight flaw with cohesive and frictional resistance, which, under far-field compression, may nucleate tension cracks at its tips, as well as produce plastic deformation there. The maximum length that the tension cracks can attain depends on the magnitude of the accompanying confining pressure (measured by the ratio, σ_2/σ_1, of the lateral pressure, σ_2, to the axial compression, σ_1) and on the overall ductility of the material that surrounds the flaw. The ductility is measured by $\varDelta = K_c/\tau_Y(\pi c)^{\frac{1}{2}}$, where K_c is the mode I fracture toughness, τ_Y is the yield stress in shear, and $2c$ is the flaw size. Whether the failure is brittle, being dominated by the growth of tension cracks, or ductile, being dominated by the growth of plastic zones, depends on the magnitude of the stress ratio, σ_2/σ_1, and the overall ductility, $\varDelta$. The influence of temperature enters implicitly through the associated values of fracture toughness, K_c, and yield stress, τ_Y. Since the former increases and the latter decreases with increasing temperature, $\varDelta$ increases with increasing temperature. It is shown that when $\varDelta$ is suitably large, the growth of tension cracks can be essentially suppressed by suitable confinement. For $\varDelta$ of the order of a few percent, however, both tension cracks and plastic deformation can occur. The model therefore seems to capture some of the essential features observed in the brittle–ductile transition process. It is shown in this paper that it also yields quantitative predictions in good accord with experimental results.

This paper is organized in the following manner. In §2 previous results on axial splitting and on faulting are reviewed, and new results of quantitative model experiments are presented, emphasizing the effect of the confining pressure: low pressure suppresses tension crack growth, resulting in the change of the failure mode from axial splitting to faulting, and high pressure suppresses the faulting. In this section, new closed-form but approximate analytic expressions are also developed for the stress intensity factors at the crack tips. By using the numerical results of the exact formulation, it is shown that the approximate expressions yield reasonable estimates over the entire range of the crack length. Next, §3 considers the micromechanics of brittle–ductile transition. In this section a two-dimensional elasticity boundary-value problem for a pre-existing flaw with associated tension cracks and plastic zones is formulated in terms of singular integral equations, the solution method is presented, numerical results are given, and their physical implications are discussed. In addition, a simple, closed-form analytic solution is presented and, by comparing its results with those of the exact formulation, it is shown that the analytic estimates are reasonably accurate when the ductility, $\varDelta$, is about 0.1 or less. In this section the results of some model experiments are also reported. These serve to illustrate the growth of plastic zones in the neighbourhood of the tips of the pre-existing flaw, under large confining pressures.

2. AXIAL SPLITTING AND FAULTING

In this section we briefly review the micromechanics of axial splitting and faulting, outline mathematical models recently developed for analysing these failure modes, and present some new, simple closed-form analytic results and some new quantitative results of model experiments.

Rocks and other materials of this kind are highly heterogeneous at the grain-scale microlevel. In granite and gabbro, for example, the constituents, such as quartz, feldspar and biotite, have considerably different mechanical properties and therefore respond differently to the applied loads. In addition these materials contain initial microdefects such as cavities and cracks. As a consequence, the imposed overall deformation is accommodated locally by extensive microcracking, which often persists even into the ductile range. The cracks are nucleated at grain boundary cavities of low aspect ratio, at the boundary of soft inclusions with easy glide, such as biotite, or at pre-existing healed cracks. In marble, on the other hand, cracks are nucleated at the intersection of lamellae or slip bands and the boundary of an adjacent unfavourably oriented crystal. Whatever the nature of such an incompatibility, it serves as a stress concentrator, resulting in microcracking. The microcracks then grow in response to the increasing applied loads, producing failure by axial splitting of the uniaxially compressed specimen (no confinement), or by faulting when the axial compression is accompanied by moderate confining pressures. The existence of the confining pressure limits the microcrack length. Microscopic studies by optical and scanning electron microscopies and by acoustic emission seem to suggest that the mechanism of overall faulting initially involves uniform nucleation and growth of microcracks throughout the sample, followed by accelerated cracking over a central region of the sample, as the peak axial compression is approached. The highly cracked region then forms the eventual macroscopic fault at axial stress values in the neighbourhood of the peak stress (see Scholz (1968), Hoshino & Koide (1970), Hallbauer *et al.* (1973), Olsson & Peng (1976), Lockner & Byerlee (1977) and Wong (1982)). Most of the microcracks are in the axial direction, and macroscopic faulting seems to occur by the linking up of an echelon of tensile microcracks. (It should be noted that there is some question whether or not the highly cracked zone which becomes the fault is formed very close to the peak stress, as reported, for example, by Hallbauer *et al.* (1973), or whether it can emerge at lower stress, as reported by Soga *et al.* (1978).)

2.1. *Mathematical model: splitting*

To model the complex micromechanisms involved in the failure of rocks in compression, it is necessary to introduce dramatic simplification and 'homogenization' of one kind or another. An essential feature of the involved physical process is that the local inhomogeneities serve as stress concentrators, promoting microcracking. This feature may be captured by a model that embeds a 'typical inhomogeneity' in an infinitely extended homogeneous solid that imposes on the inhomogeneity the constraints associated with the overall stiffness of the remaining aggregates. A rather simple two-dimensional model of this kind that lends itself to rigorous analytical calculation is a straight 'flaw' endowed with frictional resistance and cohesion, embedded in a linearly elastic homogeneous solid. In figure 1 the pre-existing flaw PP′ is sketched together with the associated curved tension cracks PQ and P′Q′, under axial and

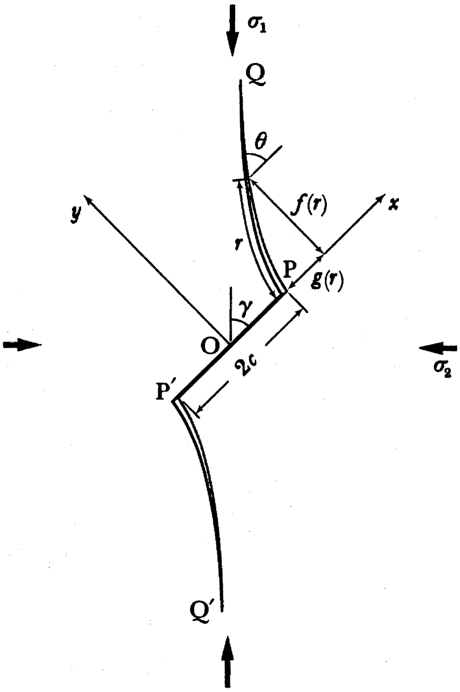

FIGURE 1. Pre-existing flaw PP′ and curved cracks PQ and P′Q′.

lateral compressions σ_1 and σ_2, $|\sigma_1| > |\sigma_2|$; compression is viewed negative. With a coordinate system x, y, as shown, the conditions on the pre-existing 'frictional and cohesive' flaw PP′, are

$$u_y^+ = u_y^-, \quad \tau_{xy} = -\tau_c + \mu\sigma_y, \tag{2.1}$$

and on the curved tension cracks PQ and P′Q′, we must have

$$\sigma_\theta = \tau_{r\theta} = 0, \tag{2.2}$$

where τ_c is the cohesive stress, μ is the coefficient of friction, σ_y is the normal and τ_{xy} is the shear stress on PP′, u_y is the displacement in the y-direction, and σ_θ and $\tau_{r\theta}$ are the polar components of the hoop and shear stresses on PQ. In (2.1) superscripts + and − refer to the value of the corresponding quantity calculated immediately above and below the x-axis, along the y-direction.

An exact formulation of this boundary-value problem has been given by Horii & Nemat-Nasser (1983, 1985*a*) in terms of singular integral equations. These singular integral equations have been solved by these authors, using the rather effective numerical scheme recently proposed by Gerasoulis & Srivastav (1981). For the sake of completeness, this exact formulation is summarized in Appendix A. Here, however, we present a closed-form, but approximate, estimate of the stress intensity factors K_{I} and K_{II} at the tips of the extended tension cracks PQ and P′Q′, when these cracks are regarded as straight lines (see figure 2*a*). This solution yields good estimates of the stress intensity factors for both small and large crack length l and is different from the analytical estimates recently developed by Ashby & Cookley (1986) and Steif (1984).

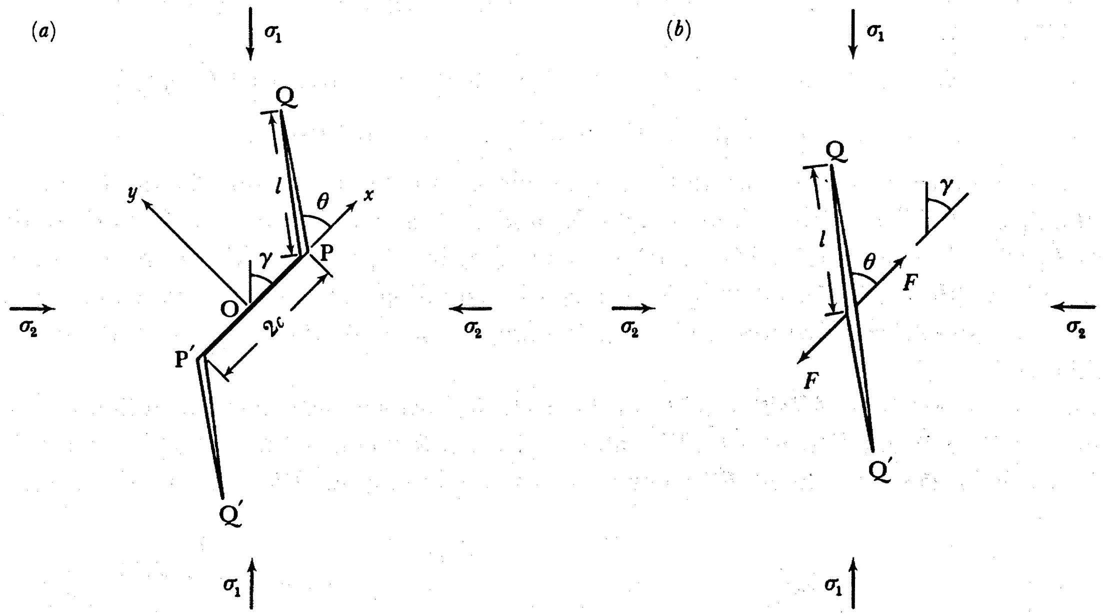

FIGURE 2. (*a*) Pre-existing flaw PP′ and straight cracks PQ and P′Q′; (*b*) a representative tension crack QQ′ with splitting forces F.

2.1.1. *Analytic estimate*

In figure 2*b* we consider a representative single crack QQ′ of length $2l$, subjected at its centre to a pair of collinear splitting forces of common magnitude F, which make an angle γ with the σ_1-direction. These forces represent the effect on the representative crack QQ′ of the sliding of the pre-existing flaw PP′, under the action of the resolved shear stress. We calculate F by estimating the driving shear stress τ^* on the pre-existing flaw, as follows:

$$\left.\begin{aligned} F &= 2c\tau^*,\\ \tau^* &= -\tfrac{1}{2}(\sigma_1-\sigma_2)\sin 2\gamma-\tau_c+\mu\tfrac{1}{2}[\sigma_1+\sigma_2-(\sigma_1-\sigma_2)\cos 2\gamma].\end{aligned}\right\} \tag{2.3}$$

The representative crack QQ′ is also subjected to the far-field stresses σ_1 and σ_2.

The stress intensity factors at Q and Q′, produced by the splitting forces, F, acting alone, are

$$K_{\mathrm{I}} = F\sin\theta/(\pi l)^{\frac{1}{2}}, \quad K_{\mathrm{II}} = -F\cos\theta/(\pi l)^{\frac{1}{2}}. \tag{2.4}$$

Although these estimates are good when l is rather large, they break down, becoming unbounded at crack initiation, when l is vanishingly small. The stress intensity factor K_{I} at crack initiation is estimated by

$$K_{\mathrm{I}} = \tfrac{3}{4}(\pi c)^{\frac{1}{2}}\tau^*(\sin\tfrac{1}{2}\theta+\sin\tfrac{3}{2}\theta), \tag{2.5}$$

where tension is taken to be positive (see Nemat-Nasser & Horii (1982, equations (A 5) and (A 6))). The maximum value of K_{I} occurs at $\theta = \theta_c = 0.392\pi$, which is a root of $\partial K_{\mathrm{I}}/\partial\theta = 0$. To match K_{I} given by $(2.4)_1$ with that given by (2.5), we introduce an *effective* crack length $2(l+l^*)$ in place of $2l$, set $(2.4)_1$ equal to (2.5) at $l = 0$ and $\theta = 0.392\pi$, and obtain $l^*/c \approx 0.27$.

Now, including the effect of the far-field stresses σ_1 and σ_2, the stress intensity factors at Q and Q′ are estimated by

$$\left.\begin{aligned} K_{\mathrm{I}} &= 2c\tau^* \sin\theta/\{\pi(l+l^*)\}^{\frac{1}{2}} + (\pi l)^{\frac{1}{2}}\tfrac{1}{2}[\sigma_1+\sigma_2-(\sigma_1-\sigma_2)\cos 2(\theta-\gamma)],\\ K_{\mathrm{II}} &= -2c\tau^* \cos\theta/\{\pi(l+l^*)\}^{\frac{1}{2}} - (\pi l)^{\frac{1}{2}}\tfrac{1}{2}(\sigma_1-\sigma_2)\sin 2(\theta-\gamma). \end{aligned}\right\} \qquad (2.6)$$

We propose to use expressions (2.6) to approximate the stress intensity factors K_{I} and K_{II} at the tips, Q and Q′, of the tension cracks PQ and P′Q′ shown in figure 2*a*. The orientation, $\theta = \theta_{\mathrm{c}}$, of these tension cracks is obtained by maximizing K_{I} in (2.6) with respect to θ. The common length, l, of PQ and P′Q′ is obtained by equating the maximum value of K_{I} with the opening-mode fracture toughness, K_{c}. It remains for us to verify the accuracy of these estimates.

Since the exact (numerical) solution of the elasticity problem associated with figure 2*a* has been given by Nemat-Nasser & Horii (1982) and Horii & Nemat-Nasser (1985*a*), the results are used in figure 3 to check the accuracy of the analytic estimates (2.6). In these figures,

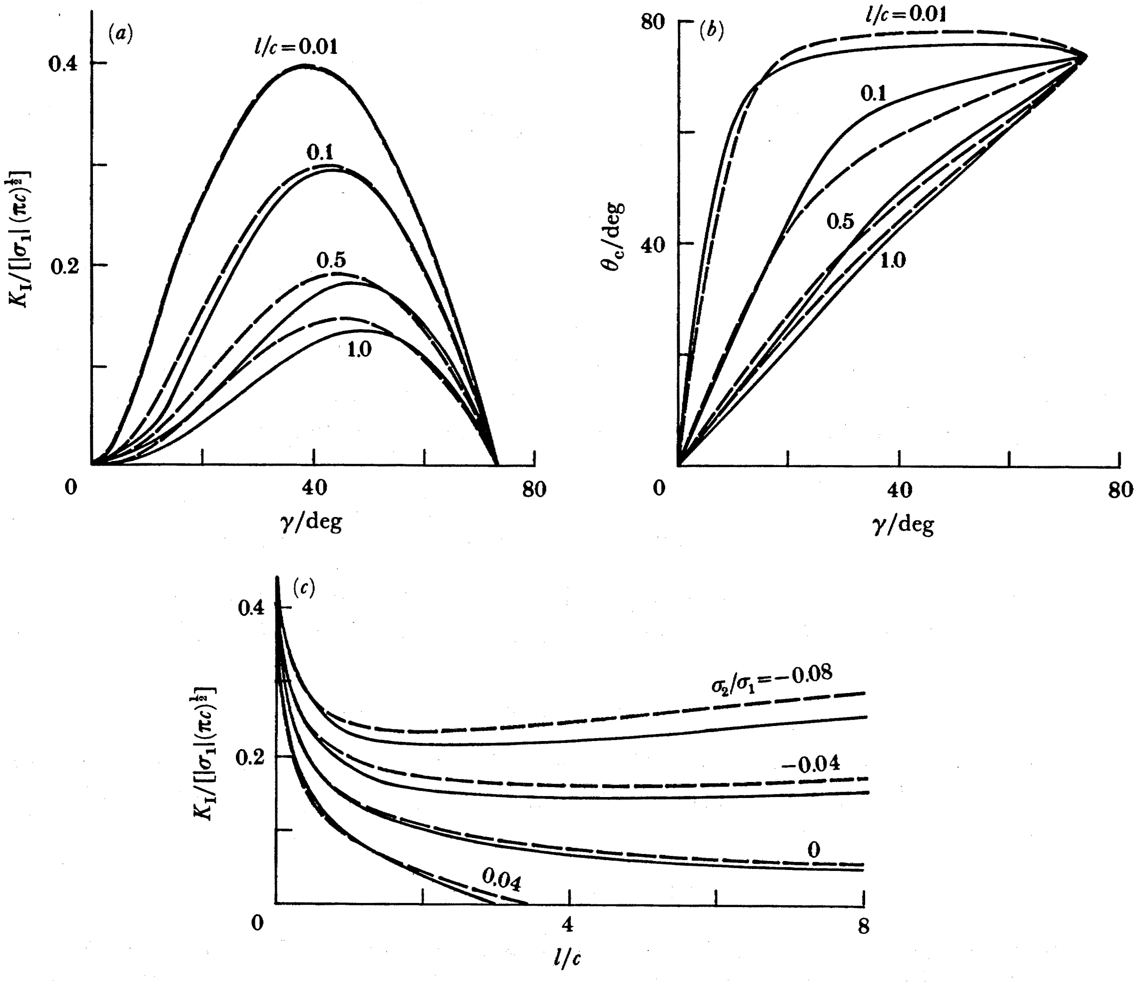

FIGURE 3. (*a*) Normalized maximum opening-mode stress intensity factor and (*b*) optimal crack orientation angle as functions of initial flaw orientation for $\mu = 0.3$, $\tau_{\mathrm{c}} = 0$, and $\sigma_2/\sigma_1 = 0$. (*c*) Normalized maximum opening-mode stress intensity factor as a function of crack length for indicated σ_2/σ_1 with $\mu = 0.3$, $\tau_{\mathrm{c}} = 0$, and $\gamma = 45°$. Solid curves are from the exact (numerical) calculation (Horii & Nemat-Nasser 1985*a*) and broken curves are from the analytic estimates (2.6).

the estimates given by (2.6) are shown by broken lines, and the exact numerical solutions are presented by solid lines. Considering the simplicity of (2.6), these analytic estimates are remarkably accurate. Note that estimates (2.6) include the effects of the cohesion, τ_c, friction, μ, and orientation, γ, of the pre-existing flaw PP′.

Even though the approximate expressions (2.6) seem to be quite accurate, the analytical results given in the remaining part of this section are all obtained from the numerical solution of the exact singular integral equations (see Appendix A).

2.1.2. *Discussion of results and model experiments*

Figure 4 displays the relation between the axial load and the length of the curved tension cracks shown in figure 1. It is seen that, under even a very small lateral confining pressure, the tension cracks emanating from the tips of the flaw grow to a finite length and then stop. On the other hand, if some lateral tension, no matter how small, accompanies axial compression, then, after a certain length is attained the crack growth becomes unstable, leading to axial splitting. Note that the axial stress required for crack initiation is inversely proportional to $c^{\frac{1}{2}}$. Hence the bigger and more compliant flaws initiate tension cracks first, i.e. at lower axial stress levels.

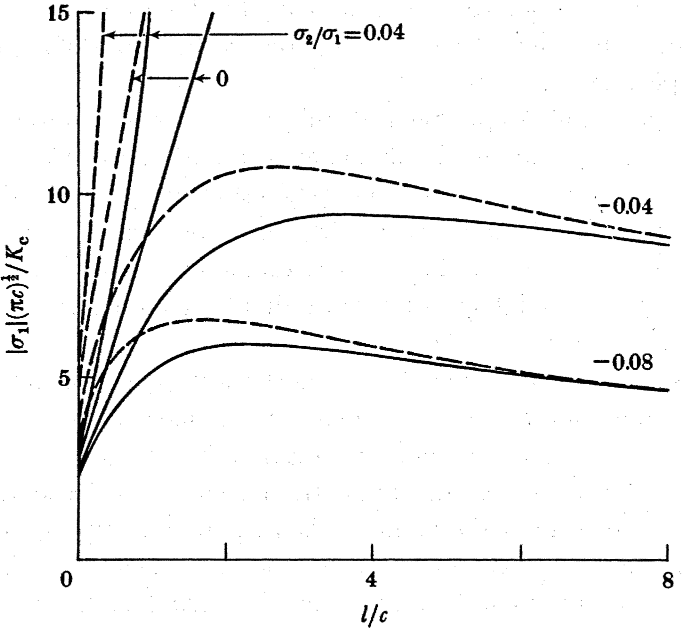

FIGURE 4. Compressive force required to attain the associated curved crack length. Solid lines, $\mu = 0.3$; broken lines, $\mu = 0.6$. (From Horii & Nemat-Nasser (1985*a*).)

To obtain insight into the process of nucleation and growth of tension cracks in homogeneous solids containing pre-existing flaws and subjected to overall compressive forces, two-dimensional model experiments have been performed. For example, Brace & Bombolakis (1963) and Hoek & Bieniawski (1965) have shown that in a glass plate containing a straight pre-existing crack oriented at an acute angle with respect to the direction of axial compression, tension cracks nucleate at the tips of this pre-existing crack, because of the relative sliding of the crack faces, and grow, curving towards the direction of axial compression. We have made a series of tests on plates 6 mm thick of Columbia resin CR39 (which is rather brittle at room temperature), containing straight slits sawn in by a blade 0.4 mm thick, and fitted with two thin brass sheets and one Teflon sheet in between, to reduce friction. The samples are held between two thick Plexiglas plates by means of lightly tightened screws, to prevent out-of-plane buckling under axial compression.

The model experiments verify the analytical results shown in figure 4. For example, in a barrel-shaped sample (two-dimensional) containing a flaw at 45° with respect to the sample axis (see figure 2*a*, *b* of Horii & Nemat-Nasser (1985*a*)), tension cracks nucleate at the tips of the slit under axial compression. These cracks then grow in a stable manner curving toward the axial direction. The barrel shape of the sample produces a small amount of lateral tension, and once a critical length is attained, spontaneous crack growth takes place, leading to axial splitting of the specimen as predicted by the results shown in figure 4. On the other hand, if the sample is in the shape of a dog bone (see figure 3*a*, *b* of Horii & Nemat-Nasser (1985*a*)), a small amount of lateral compression will accompany the axial compression, and therefore the tension cracks will attain a certain length and cease to grow after that.

Nemat-Nasser & Horii (1982) suggest that this model has a strong bearing on observed phenomena of axial splitting, exfoliation (or sheet fracture) and rockburst. They report the results of a number of model experiments that seem to support their proposal (see their figures 13–15 for exfoliation, figure 16 for rockburst, and figures 17–20 for axial splitting). These experiments all have been qualitative. Here we shall report the results of a quantitative model experiment on axial splitting.

Figure 5*a*, plate 1, shows the sample before loading. It contains a rather large number of flaws of different sizes and orientations. (In all model experiments, the flaws are 0.4 mm thick, straight slits fitted with two metal sheets and one Teflon sheet in between.) Figure 5*b*–*d* shows the specimen under overall axial compression with zero lateral confining pressure. Tension cracks nucleated at larger flaws extend in the axial direction, linking with other cracks and flaws, and the sample fails by axial splitting. Note that many smaller flaws have not even nucleated any cracks in the failed sample.

In figure 6, curve S shows the corresponding axial stress σ_1 plotted against the axial strain ϵ_1; both are shown positive, but σ_1 is compression and ϵ_1 is shortening. (Note that $\sigma_2 = 0$ in this experiment. The curve marked F in figure 6 corresponds to faulting and will be discussed in §2.4.) The points *b*–*d* marked on the stress–strain curve S correspond to figure 5*b*–*d*, respectively. Tension cracks form at the point marked S_c, after which the stress–strain curve displays pronounced nonlinearity, as more tension cracks are nucleated. The sample fails by axial splitting with a concomitant considerable drop in the axial load.

2.2. *Effect of confining pressure on failure mode*

To gain insight into the manner in which axial splitting is suppressed by confining pressure and, instead, faulting is promoted, Horii & Nemat-Nasser (1985*a*) have made a number of model experiments. Figure 7, plate 2, shows the results of one such experiment. These authors prepared two samples with an essentially identical flaw geometry, as shown in figure 7*a*. Each sample contains a number of large flaws and a row of smaller flaws. One sample is compressed axially, without any confinement. It fails by axial splitting (see figure 7*b*), caused by crack nucleation and growth at large flaws, whereas the smaller flaws do not nucleate any cracks. The second sample is axially compressed in the presence of some confinement. Initially, the large flaws nucleate cracks that grow in the direction of axial compression. Because of the

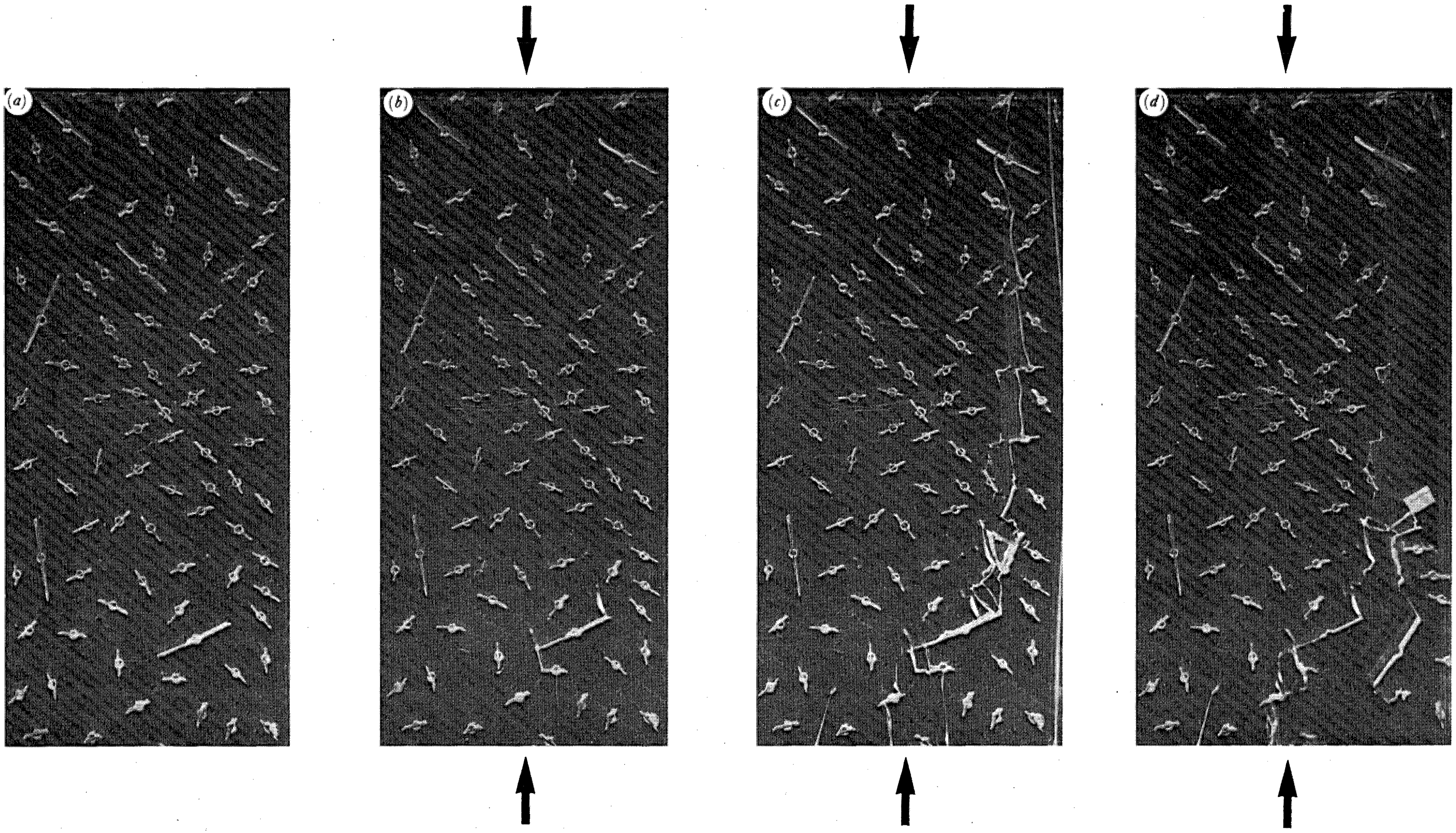

Figure 5. (a) Specimen containing a large number of flaws. (b) Under axial compression *without* confinement, cracks nucleate first at larger flaws; (c) axial splitting by the growth and coalescence of cracks; (d) shattering of a part of the specimen while many flaws in the remaining part are inactive.

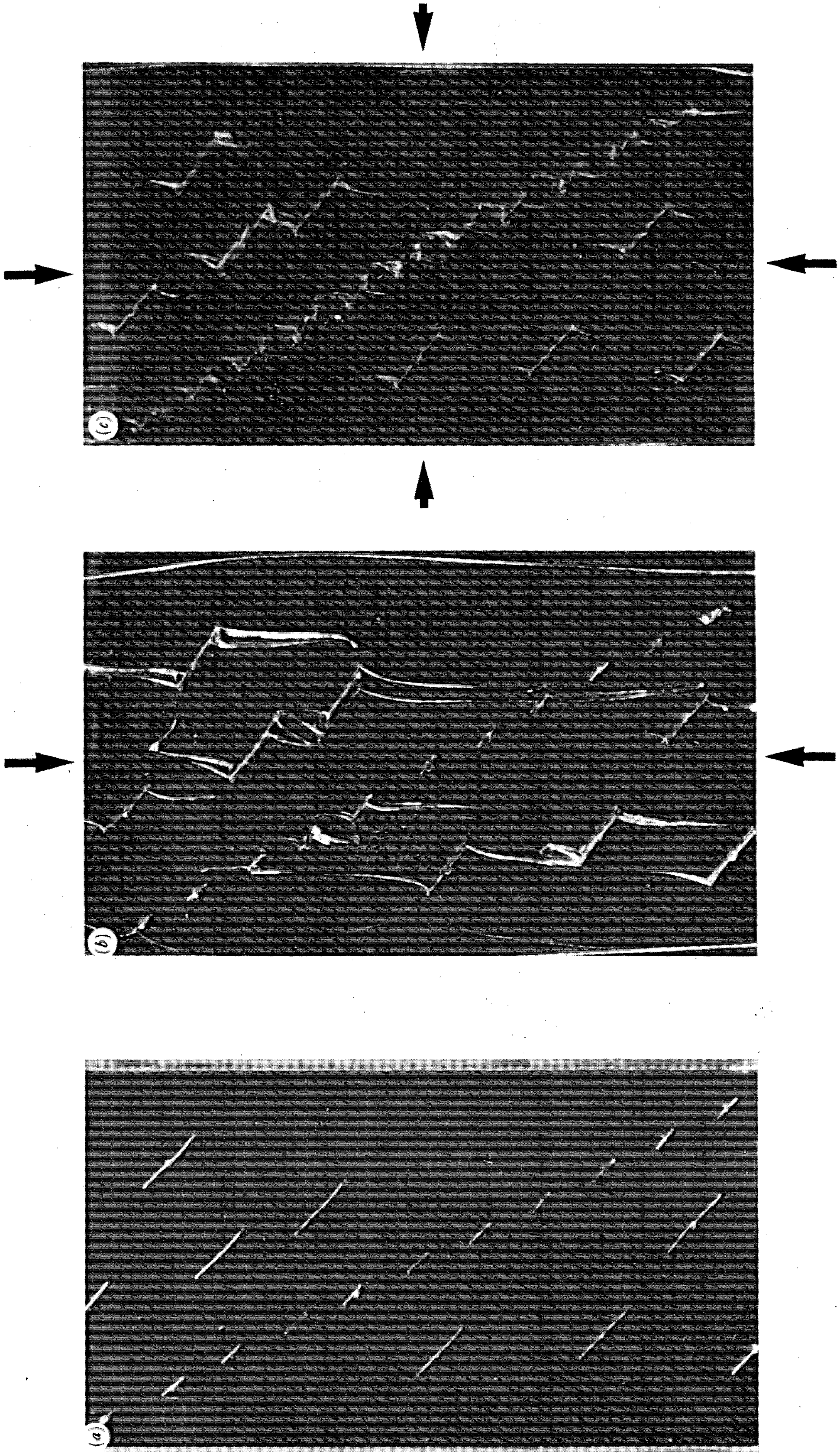

FIGURE 7. (*a*) Specimen containing a row of small flaws and several larger flaws. (*b*) Axial splitting under axial compression *without* lateral confinement; (*c*) shear failure under axial compression *with* lateral confinement. (From Horii & Nemat-Nasser (1985*a*).)

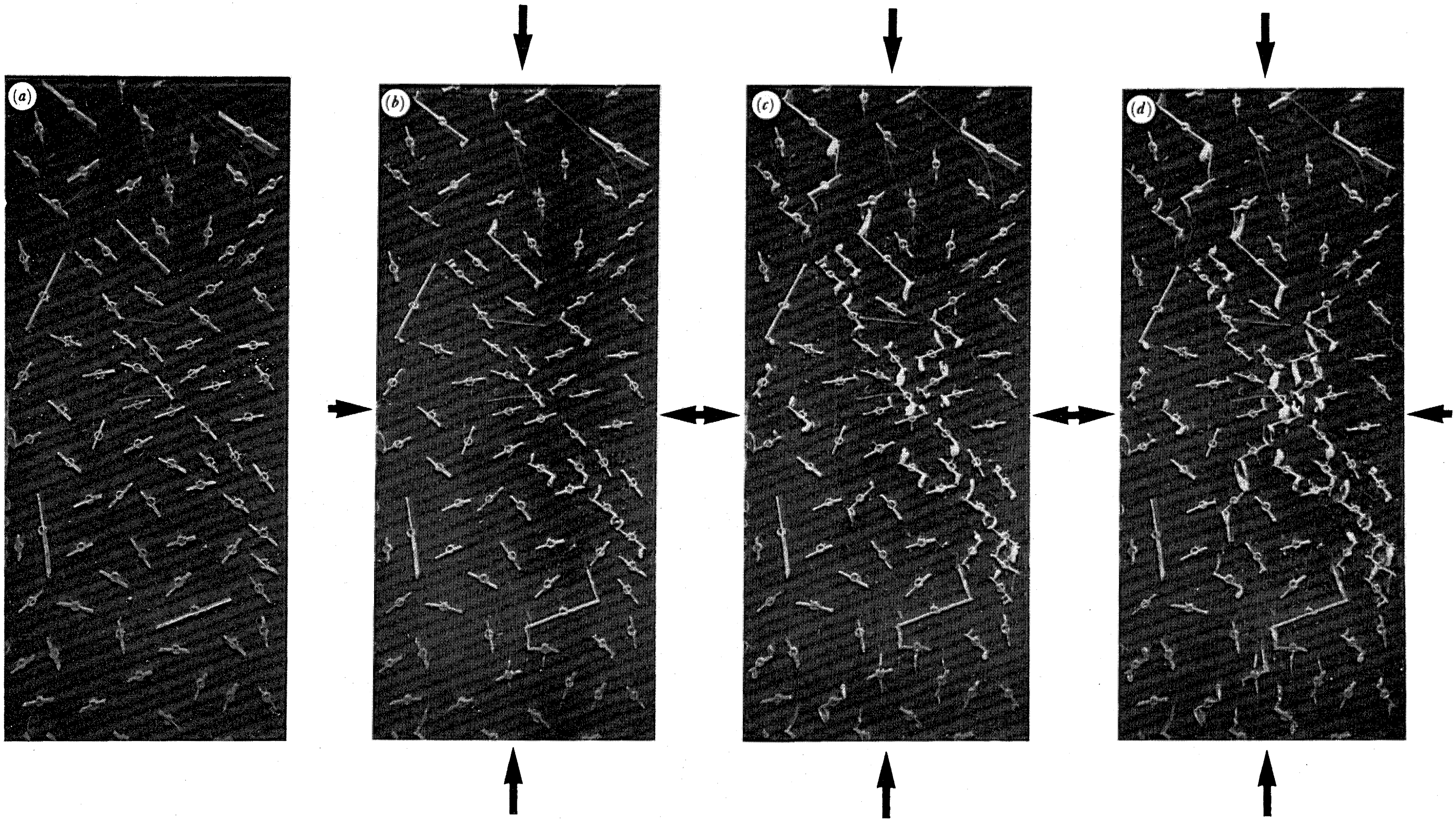

FIGURE 11. (*a*) Specimen containing a large number of flaws. (*b*) Under axial compression *with* lateral pressure $\sigma_2 = 5$ MPa, cracks nucleate at larger flaws: (*c*) cracks at larger flaws are arrested; (*d*) cracks nucleate at smaller flaws, leading to the formation of a fault.

PHILOSOPHICAL TRANSACTIONS OF THE ROYAL SOCIETY A MATHEMATICAL, PHYSICAL & ENGINEERING SCIENCES

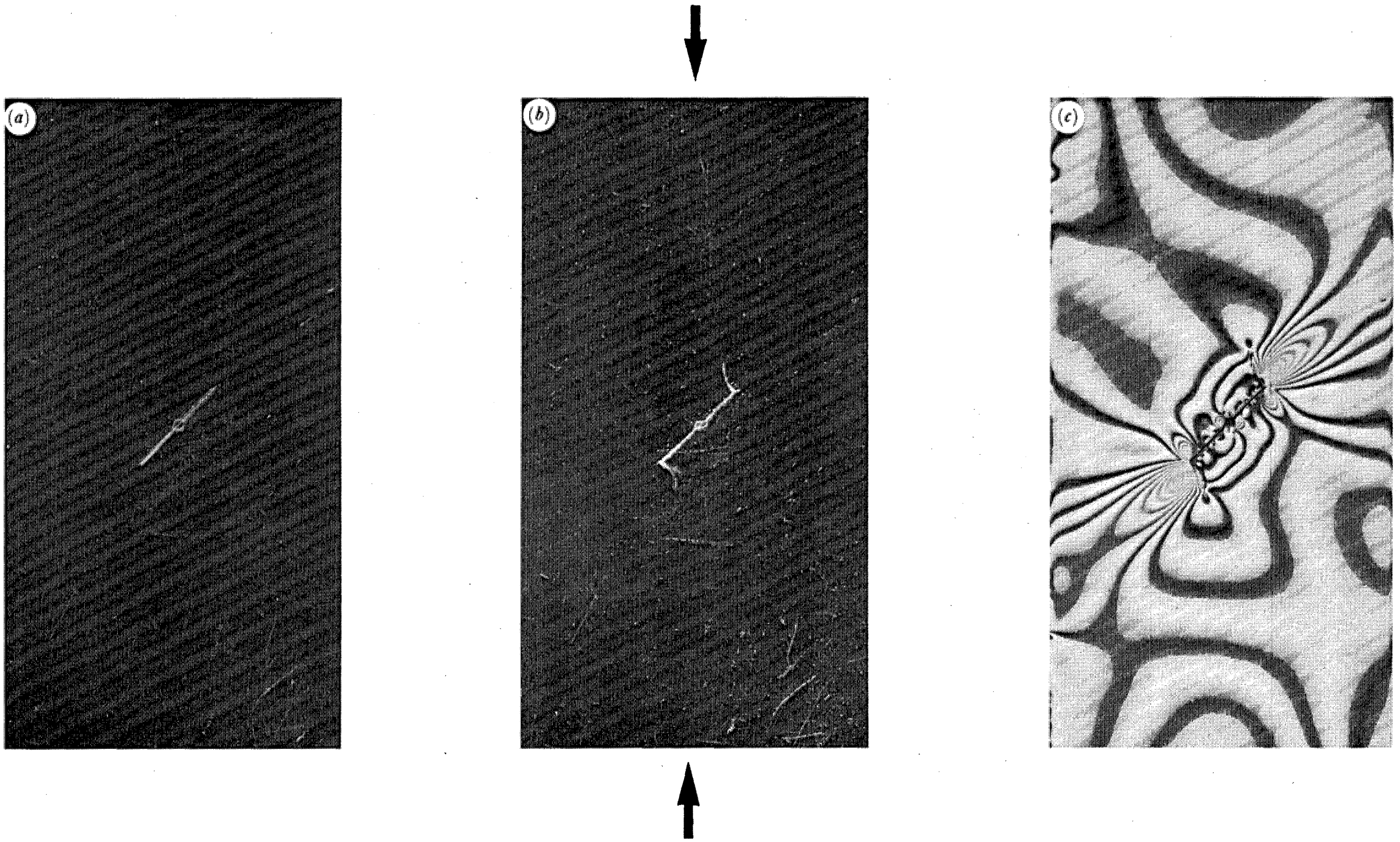

FIGURE 14. (*a*) A specimen with a pre-existing flaw. (*b*) Arrested tension cracks under axial and lateral compressive stresses of constant ratio $\sigma_2/\sigma_1 = 0.05$. (*c*) Photoelastic picture of the unloaded specimen showing the residual strain distribution.

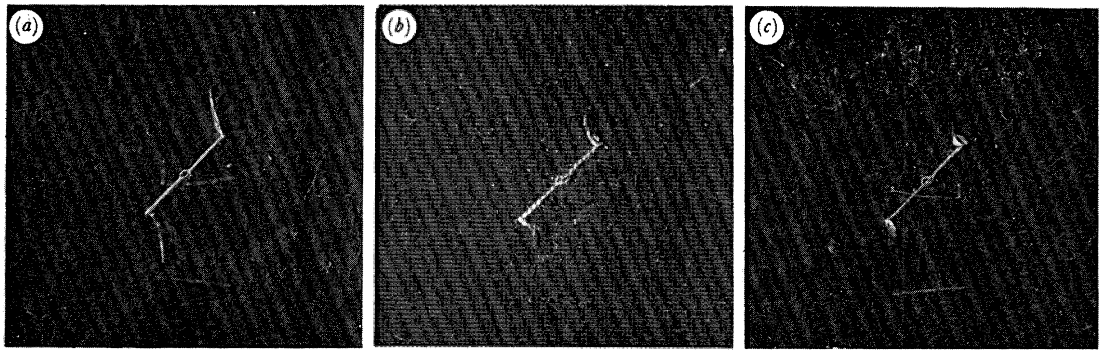

FIGURE 30. Arrested tension cracks emanating from the tips of a 1.8 cm pre-existing flaw for indicated stress ratios, σ_2/σ_1: (*a*) 0.025; (*b*) 0.05; (*c*) 0.1.

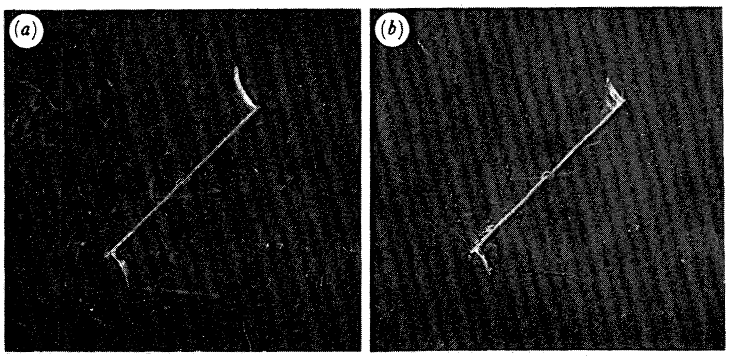

FIGURE 31. Arrested tension cracks emanating from the tips of a 3.6 cm pre-existing flaw for indicated stress ratios, σ_2/σ_1: (*a*) 0.1; (*b*) 0.15.

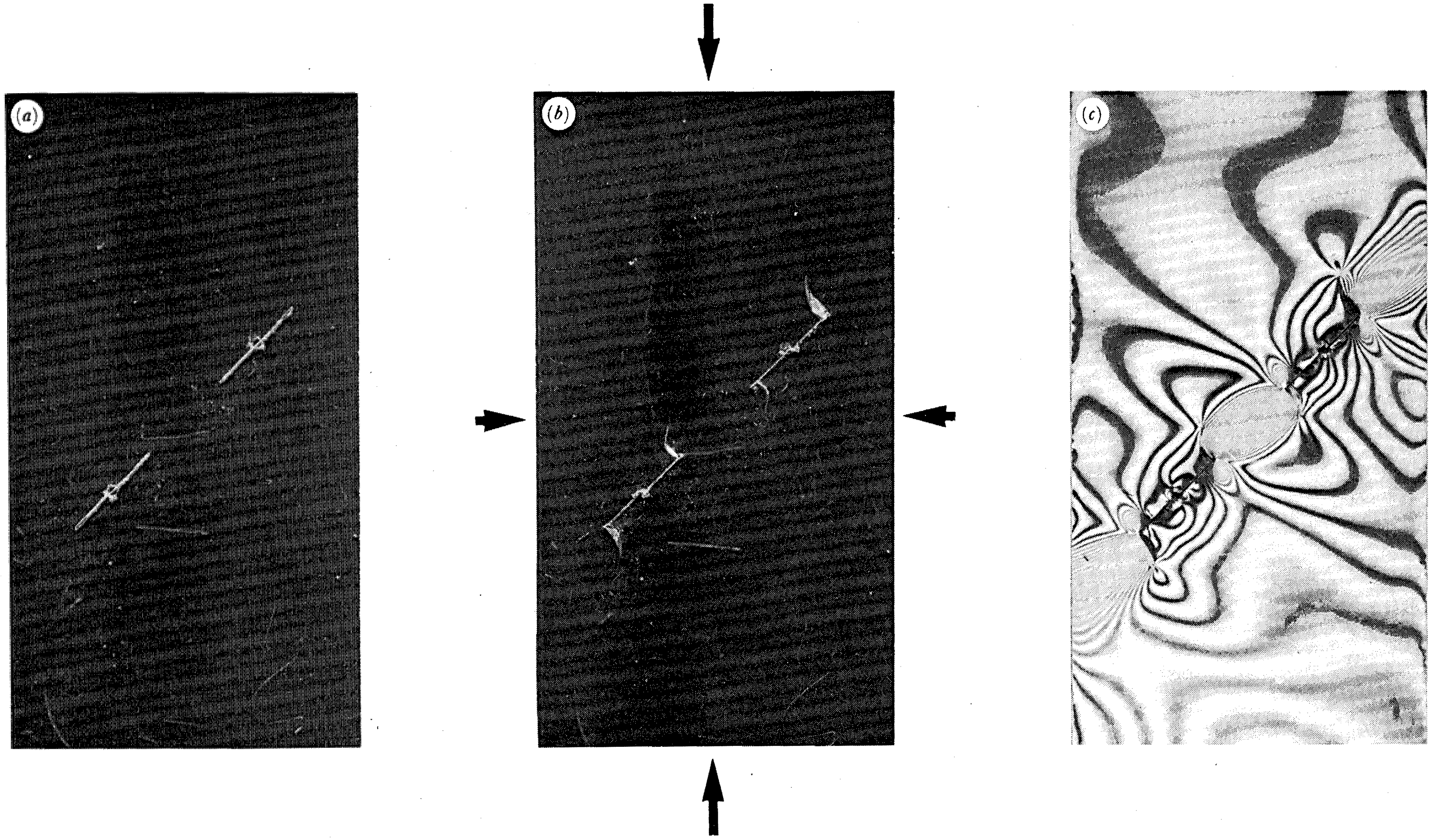

Figure 33. (*a*) A specimen with two colinear flaws. (*b*) Arrested tension cracks emanating from the ends of the flaws under axial and lateral compressive stresses of constant ratio $\sigma_2/\sigma_1 = 0.05$. (*c*) Photoelastic picture of the unloaded specimen showing the residual strain distribution.

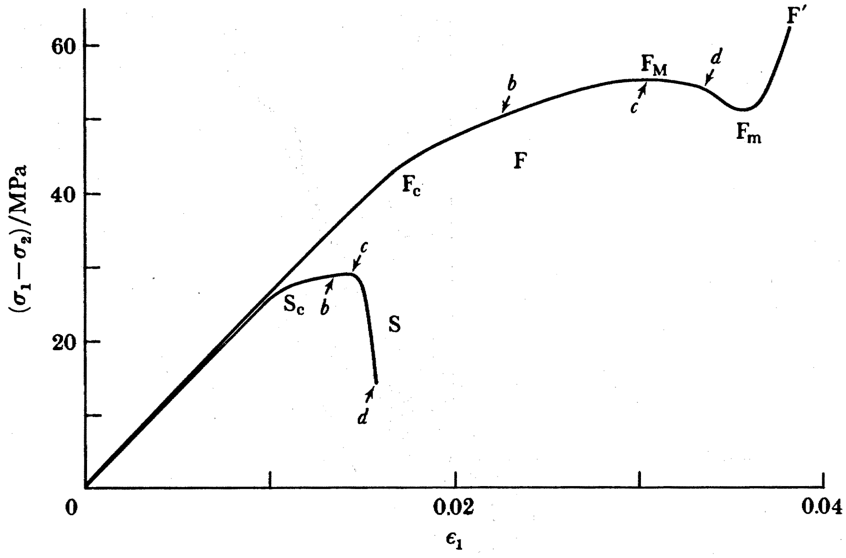

Figure 6. Stress–strain curves for specimens shown in figure 5*a*: curve S for no confinement; curve F for $\sigma_2 = 5$ MPa.

presence of confinement, these cracks are soon arrested. Then, as the axial load is further increased, tension cracks are suddenly nucleated at the tips of the smaller flaws in a row, and then these cracks grow spontaneously and simultaneously, leading to a fault (see figure 7*c*). This and related model experiments seem to support the microscopic observations of Hallbauer *et al.* (1973) who suggest that a region of high-density microcracks emerges close to the peak stress in an actual sample, and forms the eventual fault.

On the basis of these observations it is reasonable to assume that faulting is caused by the interactive growth of tension cracks at a suitable set of microflaws, the most essential ingredient being the interaction effect. A mathematical model that seems to capture this effect and, at the same time, lends itself to rigorous analysis has been proposed by Horii & Nemat-Nasser (1985*a*). In the next subsection, we briefly discuss this model and present some new, quantitative results of model experiments that support the theoretical model.

2.3. *Mathematical model: faulting*

Figure 8 shows a row of identical flaws with tension cracks at their tips. Along the flaws and the tension cracks the respective boundary conditions (2.1) and (2.2) are assumed. A typical flaw is denoted by PP′ and tension cracks at its tips by PQ and P′Q′; γ is the angle that the flaws make with respect to the σ_1-direction. The cracks make an angle θ with respect to the flaw direction. The orientation of the row with respect to the σ_1-direction is denoted by ϕ.

Because of the interaction effects, the elasticity boundary-value problem associated with this model is very complex, and its solution requires special techniques. Recently Horii & Nemat-Nasser (1985*b*) have proposed a method that they call 'the method of pseudo-tractions' for the solution of two-dimensional elasticity problems of this kind. With the aid of this method, the stress intensity factors at the tips, Q and Q′, of the cracks in figure 8 are calculated (see Appendix B for a brief account and a summary of the basic equations). The angle θ is chosen such that $K_I/|\sigma_1|(\pi c)^{\frac{1}{2}}$ is maximized.

Typical numerical results are presented in figure 9 for the basic model parameters fixed at

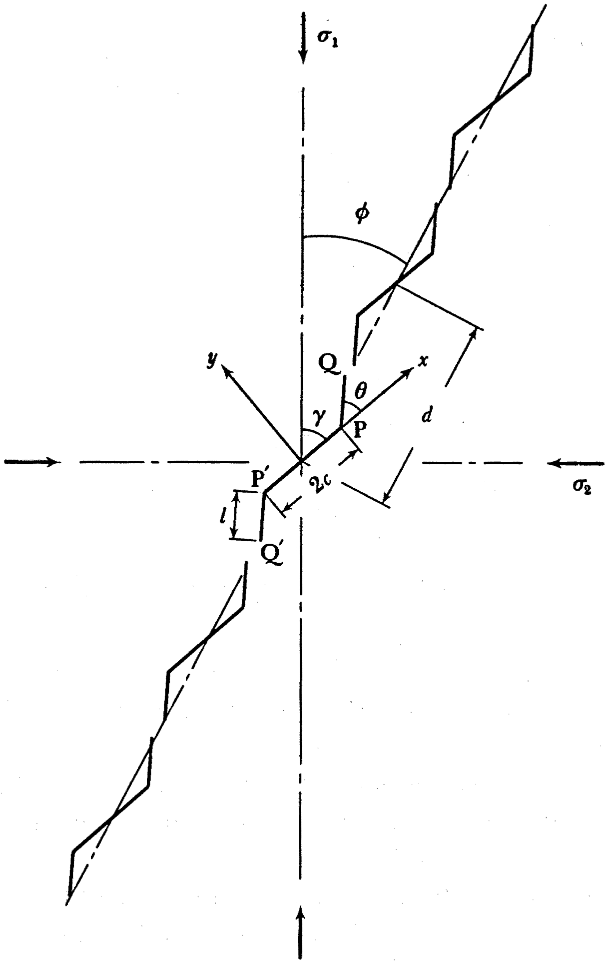

FIGURE 8. An unbounded two-dimensional solid with a row of pre-existing flaws PP′ and tension cracks PQ and P′Q′.

the following values: $|\sigma_2|(\pi c)^{\frac{1}{2}}/K_c = 0.1$, $\gamma = 43°$, and $d/c = 4$. Each curve shows the required normalized axial compression, $|\sigma_1|(\pi c)^{\frac{1}{2}}/K_c$, as a function of the crack length l/c, for indicated values of the overall orientation, ϕ, of the pre-existing flaws. When ϕ is suitably large, the variation of the axial compression with l/c is monotonic. For suitably small values of ϕ, on the other hand, the required values of the axial compression begin to decrease with increasing l/c, once a critical state is reached. For this range of the overall orientation of the flaws, tension cracks emanating from the flaw tips will suddenly grow by a finite amount at a critical value of the axial compression, producing what may be regarded as the inception of an overall fault. Horii & Nemat-Nasser (1985*a*) seek to explain and quantify rock failure by faulting in terms of this micromechanical model.

The free parameters of the model are: the orientation of the individual flaws, γ; the spacing of the flaws, d; and the orientation of the row, ϕ. Horii & Nemat-Nasser (1985*a*) assume the following simple monotonic relation between the flaw size, $2c$, and the flaw spacing, d:

$$d/c_m = b(c/c_m)^{1+a}, \quad b = d_m/c_m, \quad a > 0, \tag{2.7}$$

where $2c_m$ is the minimum flaw size with d_m being the corresponding minimum spacing. The use of a monotonic expression such as $(2.7)_1$ may be justified on the ground that in a sample

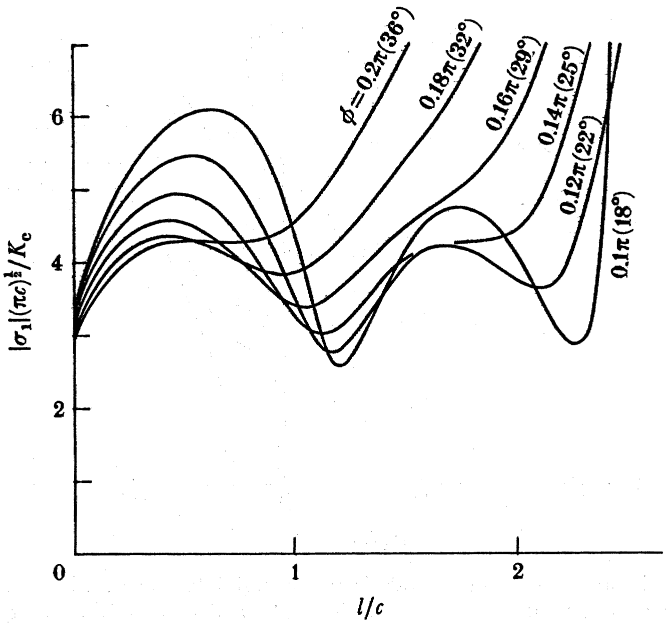

FIGURE 9. Axial stress plotted against crack length for indicated overall orientation of the row of pre-existing flaws, with $d/c = 4$, $|\sigma_2|\,(\pi c)^{\frac{1}{2}}/K_c = 0.1$, $\gamma = 43°$, and $\mu = 0.4$. (From Horii & Nemat-Nasser (1985*a*).)

of rock, for example, small flaws tend to occur more closely spaced and in greater numbers than large flaws. However (2.7) should be viewed as an arbitrary assumption employed for illustration only, and that the relation between flaw spacing and flaw size should be established by actual microscopic observation. Recent efforts by Wong (1985*a*, *b*) in this direction seem to be encouraging. At any rate, here we shall illustrate the mathematical model, using expression (2.7).

To obtain for a given confining pressure the axial compression at the inception of faulting for the mathematical model shown in figure 8, we calculate the model parameters γ, ϕ and d/c, such that the critical value of the axial compression (i.e. the value at instability) is minimized. In this manner we obtain the theoretical 'strength' curve, giving the axial compression at failure as a function of confining pressure, as well as the corresponding orientation of the fault as a function of pressure. Horii & Nemat-Nasser (1985*a*) show that the results of this mathematical model fit the experimental observations reasonably well. The parameters that must be adjusted are the exponent a and the ratio of the minimum spacing to half the minimum flaw size, $b = d_m/c_m$ in (2.7), and the fracture toughness, K_c in the expression $K_c/(\pi c_m)^{\frac{1}{2}}$, which represents an effective normalizing stress. In addition, the maximum flaw size characterized by c_M/c_m, is to be fixed, since the flaw size in the sample is bounded. Figure 10 shows the comparison between the results of the mathematical model and the data reported by Murrell (1965) on Darley Dale sandstone. For this comparison, the following values are used for the free parameters: $a = 0.18$, $b = 3.0$, $c_M/c_m = 10$, and $K_c/(\pi c_m)^{\frac{1}{2}} = 55$ MPa(8×10^3 lbf in^{-2}).

Figure 10*b* includes several theoretically obtained solid curves that require additional explanation, as follows. From the results in figure 9 it is seen that the peak value of the axial stress increases as the fault orientation, ϕ, decreases. The peak values of the axial stress corresponding to ϕ from 29° to 36° fall within a small range, i.e. $|\Delta\sigma_1|(\pi c)^{\frac{1}{2}}/K_c \approx 0.3$, above its minimum value. (This suggests that, according to the mathematical model, the overall fault

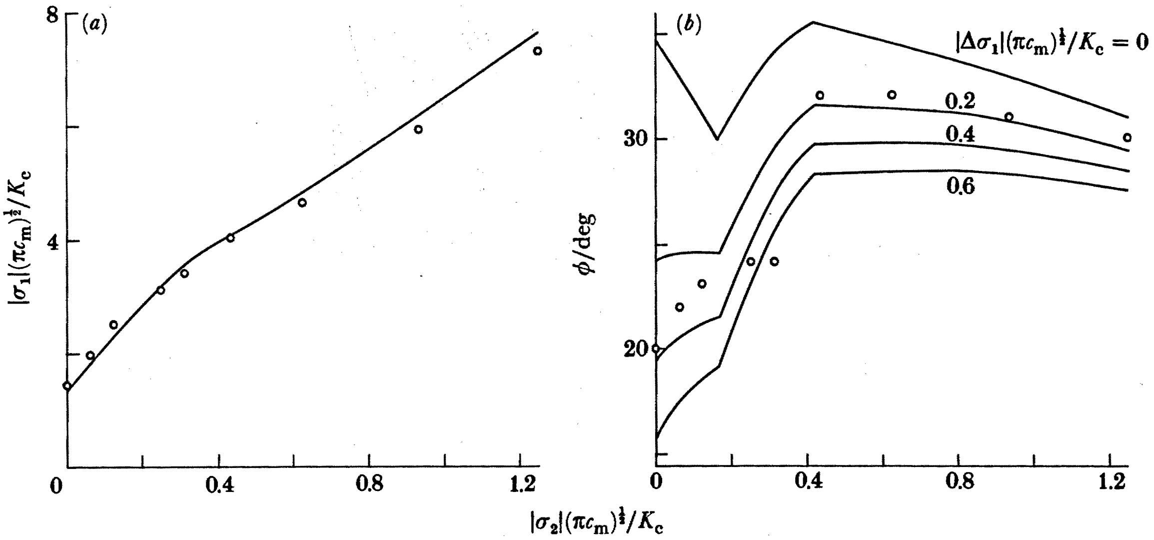

FIGURE 10. Variation of (*a*) the ultimate strength, and (*b*) the overall failure orientation with confining pressure, compared with the experimental data (points) on Darley Dale sandstone by Murrell (1965). (From Horii & Nemat-Nasser (1985*a*).)

angle should be sensitive to imperfections. In fact, experimental results by Wawersik & Brace (1971) show a variation of fault angle of about 15° in Westerly granite.) In figure 10*b* the ϕ corresponding to the indicated increment, $|\Delta\sigma_1|(\pi c_m)^{\frac{1}{2}}/K_c$, in the peak axial load beyond its minimum value, is plotted.

2.4. *Model experiment*

The curve marked by F in figure 6 is the result of an experiment on a Columbia resin CR39 plate containing a large number of initial flaws. Two such samples have been prepared (figure 5*a* and figure 11*a*, plate 3). One was tested under no confining pressure, resulting in axial splitting, as shown in figure 5*b*–*d*; see also §2.1.2 and the curve marked by S in figure 6. The second sample was tested under $\sigma_2 = 5$MPa lateral pressure, and the specimen at points *b*–*d* on the curve F is shown in figure 11*b*–*d* respectively. At point F_c on the stress–strain curve, tension cracks are first nucleated. The stress–strain curve quickly levels off as more tension cracks are produced, and a visible macroscopic fault emerges close to the peak stress (see figure 11*d*). Figure 12 shows the corresponding volumetric strain $\Delta V/V$ (positive for contraction) against the axial strain ϵ_1. After crack initiation, overall dilatancy due to microcracking is observed. In this experiment the lateral confinement has been produced by very long springs. The confining pressure remains essentially constant throughout the experiment up to the peak stress, and even after the stress drops from F_M to F_m (figure 6). However, because of the formation of faults, substantial lateral expansion occurs during the stress drop. Because of this lateral expansion, the lateral pressure begins to increase, leading to greater resistance of the sample, and hence to the portion F_mF' in figure 6. Had the confining pressure been kept at its initial constant value of $\sigma_2 = 5$ MPa, the sample would have failed with continued stress drop. Observe that the slight volume contraction indicated by the portion F_mF' in figure 12 is also triggered by the increase in the confining pressure.

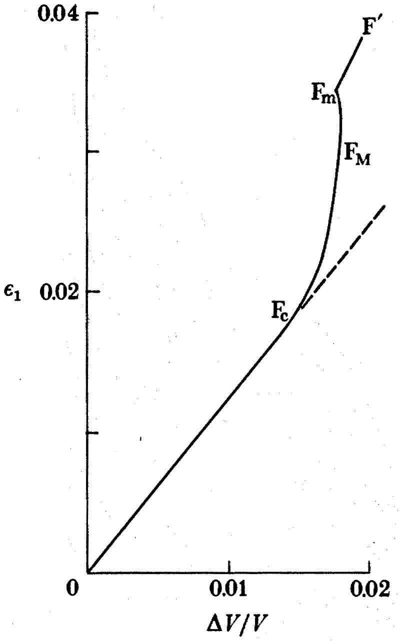

FIGURE 12. Axial strain plotted against volumetric strain for the specimen of figure 5*a* compressed axially with $\sigma_2 = 5$ MPa.

3. BRITTLE–DUCTILE TRANSITION

Brittle failure by faulting is suppressed by sufficiently high confining pressures that promote more or less uniformly distributed inelastic deformation throughout the sample. Microscopically, however, the deformation remains highly heterogeneous, in view of the microstructure of the material. Depending on the material and the temperature, the inelastic deformation may stem from grain-size microcracking, plastic glide, or a combination of the two. For example, in marble and limestone, as well as in pyroxenes, microcracking and the associated cataclastic flow can be inhibited at room temperature by large enough confining pressures, whereas for other materials, such as quartz and feldspar, this requires higher temperatures (Donath *et al.* 1971; Tobin & Donath 1971; Olsson & Peng 1976; Tullis & Yund 1977; Kirby & Kronenberg 1984). In this section we present a simple mathematical model that seems to capture the essence of these processes, compare the consequences of the model with experimental results, and show that good qualitative and quantitative correlations are obtained. In addition we support the mathematical model by some simple laboratory model experiments.

Before discussing the mathematical model it is instructive to examine the influence of increasing lateral pressure on the interactive, unstable crack growth associated with a row of pre-existing flaws, shown in figure 8 and discussed in §§2.3 and 2.4. For $\phi = 29°$, $\gamma = 43°$, and $d/c = 4$, the results are shown in figure 13. It is seen that increasing the lateral pressure suppresses the unstable growth of tension cracks emanating from the tips of the interacting flaws, and therefore the associated faulting.

Figure 14*a*, plate 4, shows a single flaw in a Columbia resin CR39 plate. The specimen is compressed with constant stress ratio $\sigma_2/\sigma_1 = 0.05$. Because of the presence of the lateral confinement, σ_2, the growth of tension cracks emanating from the tips of the flaw is arrested after a finite crack length is attained (see figure 14*b*). The residual strain distribution in the

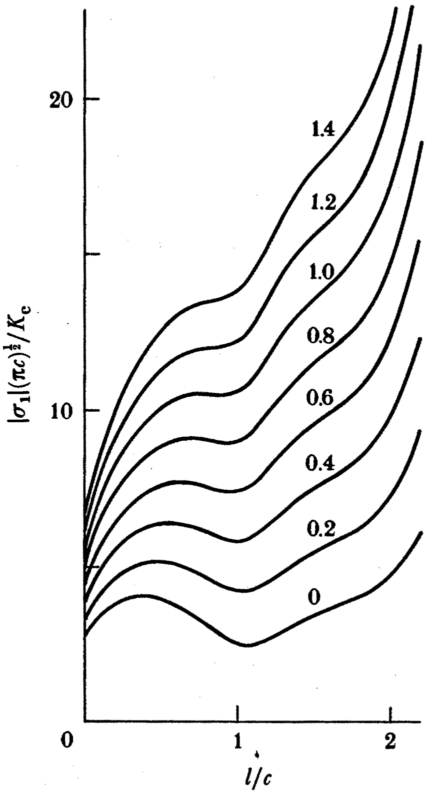

FIGURE 13. Compressive force required to attain the associated length of cracks emanating from a row of pre-existing flaws, under the indicated normalized lateral stresses (contours of $|\sigma_2|(\pi c)^{\frac{1}{2}}/K_c$), with $d/c = 4$, $\gamma = 43°$ and $\phi = 29°$.

unloaded specimen is shown by the photoelastic picture of figure 14*c*. It is seen that extensive plastic flow has occurred parallel to the pre-existing flaw, near its tips. On the basis of this observation we shall present in this section a simple but effective mathematical model for brittle–ductile transition.

3.1. *Mathematical model: brittle–ductile transition*

The mathematical model is shown in figure 15. It consists of the frictional and cohesive flaw PP′ which has produced, at its tips, out-of-plane tension cracks PQ and P′Q′ of common length l_t, as well as collinear plastic slips PR and P′R′ of common length l_p. The boundary conditions on the pre-existing flaw and the tension cracks are given, respectively, by (2.1) and (2.2). The conditions on the slip lines PR and P′R′ are

$$u_y^+ = u_y^-, \quad \tau_{xy} = -\tau_Y, \tag{3.1}$$

where τ_Y is the yield stress in shear. The principal stresses at infinity are prescribed to be σ_1 and σ_2. In this model the tension cracks are assumed to be straight; this is a good approximation to the curved cracks like the ones shown in figure 1, as demonstrated by Horii & Nemat-Nasser (1985*a*). The plastic zones are modelled by dislocation lines collinear with the pre-existing flaw, as motivated by the model experiments, although it is not difficult to consider a non-collinear dislocation line or several such lines, depending on the circumstances. For a single, isolated flaw, the use of collinear dislocation lines is reasonable and seems to yield adequate results.

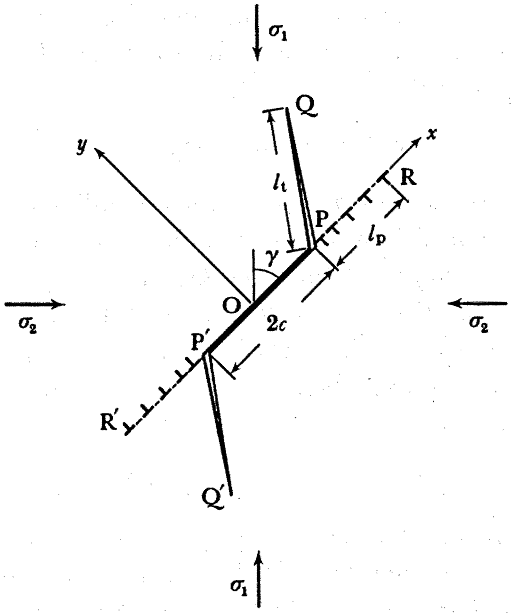

FIGURE 15. Pre-existing flaw PP′, tension cracks PQ and P′Q′, and plastic zones PR and P′R′.

The stresses at the ends of the plastic zones must be bounded. We seek a solution that renders the mode II stress intensity factor at R and R′ zero, i.e. we require

$$K_{\mathrm{II}}^{\mathrm{R}} = 0, \quad \text{at R and R}'. \tag{3.2}$$

In what follows, we first present in §3.2 an exact formulation of the boundary-value problem shown in figure 15 in terms of singular integral equations that can be solved numerically to any desired degree of accuracy. We then use in §3.4 the numerical results presented in §3.3 to examine the physical implications of the proposed model. In §3.5 results of our model experiments are compared with analytical results, and experimental observations on the brittle–ductile transition of actual rocks are discussed. Finally, in §3.6 we present a simple closed-form analytic solution of the boundary-value problem shown in figure 15 and, by comparing results with those from the exact solution, show that this analytic estimate yields reasonably accurate results. The reader who may not be interested in the detailed mathematical formulation may skip §3.2 without a loss of continuity.

3.2. *Exact formulation*

For the exact formulation of the elasticity boundary-value problem (figure 15), Muskhelishvili's (1953) complex stress functions Φ and Ψ are employed. In terms of these potentials, the stresses and displacements are given by

$$\left.\begin{aligned} \sigma_x+\sigma_y &= 2(\Phi'+\overline{\Phi'}), \\ \sigma_y-\sigma_x+2\mathrm{i}\tau_{xy} &= 2(\bar{z}\Phi''+\Psi'), \\ 2G(u_x+\mathrm{i}u_y) &= \kappa\Phi-z\overline{\Phi'}-\overline{\Psi}, \end{aligned}\right\} \tag{3.3}$$

where G is the shear modulus; $\kappa = 3\text{–}4\,\nu$ for plane strain and $\kappa = (3-\nu)/(1+\nu)$ for plane stress, ν being Poisson's ratio; $z = x+\mathrm{i}y$ with $\mathrm{i} = \surd -1$; the overbar denotes the complex conjugate; and prime stands for differentiation with respect to the argument.

To solve the boundary-value problem, we introduce stress functions $\Phi^{\mathrm{D}} = \Phi_0 + \Phi_{\mathrm{R}}$ and $\Psi^{\mathrm{D}} = \Psi_0 + \Psi_{\mathrm{R}}$ for a pair of antisymmetric dislocations at z_0 and $-z_0$ in the complex z-plane, which satisfy the following conditions along PP′:

$$\tau_0 + \tau_{\mathrm{R}} = \mu\sigma_0, \quad \sigma_{\mathrm{R}} = 0, \tag{3.4}$$

where σ_0 and τ_0 are the normal and shear stresses corresponding to the stress functions Φ_0 and Ψ_0 for the pair of antisymmetric dislocations in an infinite plane, and σ_{R} and τ_{R} are the stresses associated with the supplementary stress functions Φ_{R} and Ψ_{R}. The functions Φ_{R} and Ψ_{R} are obtained in such a manner that the prescribed stress conditions (3.4) on the pre-existing flaw PP′ are satisfied. In addition, we have the stress functions $\Phi^{\infty} = \Phi_0^{\infty} + \Phi_{\mathrm{R}}^{\infty}$ and $\Psi^{\infty} = \Psi_0^{\infty} + \Psi_{\mathrm{R}}^{\infty}$ for the prescribed stresses at infinity. These stress functions must be such that the following conditions are satisfied along PP′:

$$\tau_{xy}^{\infty} + \tau_{\mathrm{R}}^{\infty} = -\tau_{\mathrm{c}} + \mu\sigma_y^{\infty}, \quad \sigma_{\mathrm{R}}^{\infty} = 0, \tag{3.5}$$

where τ_{xy}^{∞} and σ_y^{∞} are stress components at infinity corresponding to the stress functions Φ_0^{∞} and Ψ_0^{∞}, and $\sigma_{\mathrm{R}}^{\infty}$ and $\tau_{\mathrm{R}}^{\infty}$ are the normal and shear stresses due to the supplementary stress functions $\Phi_{\mathrm{R}}^{\infty}$ and $\Psi_{\mathrm{R}}^{\infty}$. Note that $(3.4)_2$ and $(3.5)_2$, together with (3.10), are sufficient to satisfy the continuity conditions $(2.1)_1$.

The stress potentials Φ'_{R} and Ψ'_{R}, and $\Phi_{\mathrm{R}}^{\infty\prime}$ and $\Psi_{\mathrm{R}}^{\infty\prime}$, that satisfy (3.4) and (3.5), respectively, are obtained by the method of Muskhelishvili (1953); see, for example, Lo (1978) and Nemat-Nasser (1983). The stress potentials are given as follows:

$$\left.\begin{aligned}
&\Phi_0 = \alpha \ln \frac{z-z_0}{z+z_0}, \quad \Psi_0 = \bar{\alpha} \ln \frac{z-z_0}{z+z_0} - \alpha \overline{z_0} \frac{2z}{z^2-z_0^2},\\
&\Phi'_{\mathrm{R}} = (\overline{\alpha\beta} - \alpha\beta)\,[F(z,z_0) + F(z,\overline{z_0})] + (\overline{z_0} - z_0)\,[\alpha\overline{\beta}G(z,z_0) + \bar{\alpha}\beta G(z,\overline{z_0})],\\
&\Psi'_{\mathrm{R}} = \overline{\Phi}'_{\mathrm{R}} - \Phi'_{\mathrm{R}} - z\Phi''_{\mathrm{R}},\\
&\Phi_0^{\infty\prime} = \tfrac{1}{4}(\sigma_1+\sigma_2), \quad \Psi_0^{\infty\prime} = -\tfrac{1}{2}(\sigma_1-\sigma_2)\,\mathrm{e}^{-2\mathrm{i}\gamma},\\
&\Phi_{\mathrm{R}}^{\infty\prime} = \tfrac{1}{2}(\tau_{xy}^{\infty} - \mu\sigma_y^{\infty} + \tau_{\mathrm{c}})\,\mathrm{i}[1 - z/(z^2-c^2)^{\frac{1}{2}}],\\
&\Psi_{\mathrm{R}}^{\infty\prime} = \tfrac{1}{2}(\tau_{xy}^{\infty} - \mu\sigma_y^{\infty} + \tau_{\mathrm{c}})\,\mathrm{i}[-zc^2/(z^2-c^2)^{\frac{3}{2}} + 2z/(z^2-c^2)^{\frac{1}{2}} - 2],
\end{aligned}\right\} \tag{3.6}$$

with

$$\left.\begin{aligned}
F(z,z_0) &= \left[1 - \frac{z}{z_0}\frac{(z_0^2-c^2)^{\frac{1}{2}}}{(z^2-c^2)^{\frac{1}{2}}}\right]\frac{z_0}{z^2-z_0^2},\\
G(z,z_0) &= \frac{\partial}{\partial z_0}F(z,z_0)\\
&= \left[1 - \frac{z}{z_0}\frac{(z_0^2-c^2)^{\frac{1}{2}}}{(z^2-c^2)^{\frac{1}{2}}}\right]\frac{2z_0^2}{(z^2-z_0^2)^2} + \left[1 - \frac{zz_0}{(z_0^2-c^2)^{\frac{1}{2}}(z^2-c^2)^{\frac{1}{2}}}\right]\Big/(z^2-z_0^2),
\end{aligned}\right\} \tag{3.7}$$

where $\alpha = G([u_r] + \mathrm{i}[u_\theta])\,\mathrm{e}^{\mathrm{i}\theta}/\pi\mathrm{i}(\kappa+1)$, $[u] = u^+ - u^-$, $\beta = \frac{1}{2}(1+\mathrm{i}\mu)$, and $\overline{\Phi} = \overline{\Phi(\bar{z})}$. From (3.4) and (3.5) it is seen that the stress functions $\Phi = \Phi^{\mathrm{D}} + \Phi^{\infty}$ and $\Psi = \Psi^{\mathrm{D}} + \Psi^{\infty}$ satisfy the second condition of (2.1). Hence any collection of dislocations of the kind considered above will automatically satisfy $(2.1)_2$.

Suitably distributed dislocations of densities $\alpha_{\mathrm{t}}(r)$ and $\alpha_{\mathrm{p}}(t)$ are now introduced to represent the tension cracks, PQ and P′Q′, and the plastic zones, PR and P′R′, respectively; $\alpha_{\mathrm{t}}(r)$ is a complex function of $r (0 \leqslant r \leqslant l_{\mathrm{t}})$ defined on the tension crack PQ; $\alpha_{\mathrm{p}}(t)$ is a function of

$t(0 \leqslant t \leqslant l_p)$ defined on the plastic zone PR; it takes on purely imaginary values, so that the first condition of (3.1) is ensured. Since

$$\sigma_\theta + \mathrm{i}\tau_{r\theta} = \Phi' + \overline{\Phi'} + \mathrm{e}^{2\mathrm{i}\theta}(\bar{z}\Phi'' + \Psi'), \tag{3.8}$$

it follows from $(2.2)_2$ and $(3.1)_2$ that

$$\left.\begin{aligned}
&\int_0^{l_t} [\Phi_{tt}^{D\prime} + \overline{\Phi_{tt}^{D\prime}} + \mathrm{e}^{2\mathrm{i}\theta}(\overline{z_t}\,\Phi_{tt}^{D\prime\prime} + \Psi_{tt}^{D\prime})]\,\mathrm{d}r + \int_0^{l_p} [\Phi_{pt}^{D\prime} + \overline{\Phi_{pt}^{D\prime}} + \mathrm{e}^{2\mathrm{i}\theta}(\overline{z_t}\,\Phi_{pt}^{D\prime\prime} + \Psi_{pt}^{D\prime})]\,\mathrm{d}t \\
&\qquad\qquad + \Phi_t^{\infty\prime} + \overline{\Phi_t^{\infty\prime}} + \mathrm{e}^{2\mathrm{i}\theta}(\overline{z_t}\,\Phi_t^{\infty\prime\prime} + \Psi_t^{\infty\prime}) = 0, \quad \text{on} \quad \mathrm{PQ}\ (0 \leqslant s \leqslant l_t), \\
&\mathrm{Im}\left\{\int_0^{l_p} [\Phi_{pp}^{D\prime} + \overline{\Phi_{pp}^{D\prime}} + \overline{z_p}\,\Phi_{pp}^{D\prime\prime} + \Psi_{pp}^{D\prime}]\,\mathrm{d}t + \int_0^{l_t} [\Phi_{tp}^{D\prime} + \overline{\Phi_{tp}^{D\prime}} + \overline{z_p}\,\Phi_{tp}^{D\prime\prime} + \Psi_{tp}^{D\prime}]\,\mathrm{d}r\right. \\
&\qquad\qquad \left. + \Phi_p^{\infty\prime} + \overline{\Phi_p^{\infty\prime}} + \overline{z_p}\,\Phi_p^{\infty\prime\prime} + \Psi_p^{\infty\prime}\right\} = -\tau_Y, \quad \text{on} \quad \mathrm{PR}\ (0 \leqslant u \leqslant l_p),
\end{aligned}\right\} \tag{3.9}$$

where $z_t = c + s\,\mathrm{e}^{\mathrm{i}\theta}$, $z_p = c + u$,

$$\Phi_{tt}^D = \Phi^D(c + s\,\mathrm{e}^{\mathrm{i}\theta}, c + r\,\mathrm{e}^{\mathrm{i}\theta}; \alpha_t(r)), \quad \Psi_{tt}^D = \Psi^D(c + s\,\mathrm{e}^{\mathrm{i}\theta}, c + r\,\mathrm{e}^{\mathrm{i}\theta}; \alpha_t(r)),$$

$$\Phi_{pt}^D = \Phi^D(c + s\,\mathrm{e}^{\mathrm{i}\theta}, c + t; \alpha_p(t)), \quad \Psi_{pt}^D = \Psi^D(c + s\,\mathrm{e}^{\mathrm{i}\theta}, c + t; \alpha_p(t)),$$

$$\Phi_{tp}^D = \Phi^D(c + u, c + r\,\mathrm{e}^{\mathrm{i}\theta}; \alpha_t(r)), \quad \Psi_{tp}^D = \Psi^D(c + u, c + r\,\mathrm{e}^{\mathrm{i}\theta}; \alpha_t(r)),$$

$$\Phi_{pp}^D = \Phi^D(c + u, c + t; \alpha_p(t)), \quad \Psi_{pp}^D = \Psi^D(c + u, c + t; \alpha_p(t)),$$

$$\Phi_t^\infty = \Phi^\infty(c + s\,\mathrm{e}^{\mathrm{i}\theta}), \quad \Psi_t^\infty = \Psi^\infty(c + s\,\mathrm{e}^{\mathrm{i}\theta}), \quad \Phi_p^\infty = \Phi^\infty(c + u), \quad \text{and} \quad \Psi_p^\infty = \Psi^\infty(c + u),$$

with $\Phi^D(z, z_0; \alpha)$, $\Psi^D(z, z_0; \alpha)$, $\Phi^\infty(z)$, and $\Psi^\infty(z)$ given in (3.6); Im $\{A\}$ stands for the imaginary part of A. (The stress function Φ^D depends on two independent complex variables, z_0 and z, which respectively denote the position of the dislocation and the point at which Φ^D is evaluated. In addition, Φ^D depends on the dislocation density α; hence we have written $\Phi^D(z_0, z; \alpha)$.)

The first condition of (2.1) requires

$$\int_0^{l_t} [\alpha_t(r) + \overline{\alpha_t(r)}]\,\mathrm{d}r = 0. \tag{3.10}$$

Equation (3.9) can be rewritten as

$$\left.\begin{aligned}
&\int_0^{l_t} \frac{2\,\mathrm{e}^{\mathrm{i}\theta}\overline{\alpha_t(r)}}{s - r}\,\mathrm{d}r + \int_0^{l_t} L(c + s\,\mathrm{e}^{\mathrm{i}\theta}, c + r\,\mathrm{e}^{\mathrm{i}\theta}; \alpha_t(r), \theta)\,\mathrm{d}r \\
&\quad + \int_0^{l_p} \left\{\alpha_p(t)\left[\frac{1}{s\,\mathrm{e}^{\mathrm{i}\theta} - t} - \frac{(s\,\mathrm{e}^{-\mathrm{i}\theta} - t)\,\mathrm{e}^{2\mathrm{i}\theta}}{(s\,\mathrm{e}^{\mathrm{i}\theta} - t)^2}\right] + \overline{\alpha_p(t)}\left[\frac{1}{s\,\mathrm{e}^{-\mathrm{i}\theta} - t} + \frac{\mathrm{e}^{2\mathrm{i}\theta}}{s\,\mathrm{e}^{\mathrm{i}\theta} - t}\right]\right\}\mathrm{d}t \\
&\qquad\qquad + \int_0^{l_p} L(c + s\,\mathrm{e}^{\mathrm{i}\theta}, c + t; \alpha_p(t), \theta)\,\mathrm{d}t + \Phi_t^{\infty\prime} + \overline{\Phi_t^{\infty\prime}} + \mathrm{e}^{2\mathrm{i}\theta}(\overline{z_t}\,\Phi_t^{\infty\prime\prime} + \Psi_t^{\infty\prime}) = 0, \\
&\qquad\qquad\qquad\qquad\qquad\qquad\qquad\qquad\qquad\qquad \text{for} \quad 0 \leqslant s \leqslant l_t, \\
&\int_0^{l_p} \frac{2\overline{\alpha_p(t)}}{s - t}\,\mathrm{d}t + \int_0^{l_p} L(c + u, c + t; \alpha_p(t), 0)\,\mathrm{d}t \\
&\quad + \mathrm{i}\,\mathrm{Im}\left\{\int_0^{l_t} \left\{\alpha_t(r)\left[\frac{1}{u - r\,\mathrm{e}^{\mathrm{i}\theta}} - \frac{u - r\,\mathrm{e}^{-\mathrm{i}\theta}}{(u - r\,\mathrm{e}^{\mathrm{i}\theta})^2}\right] + \overline{\alpha_t(r)}\left[\frac{1}{u - r\,\mathrm{e}^{-\mathrm{i}\theta}} + \frac{1}{u - r\,\mathrm{e}^{\mathrm{i}\theta}}\right]\right\}\mathrm{d}r\right. \\
&\qquad\qquad \left. + \int_0^{l_t} L(c + u, c + r\,\mathrm{e}^{\mathrm{i}\theta}; \alpha_t(r), 0)\,\mathrm{d}r + \Phi_p^{\infty\prime} + \overline{\Phi_p^{\infty\prime}} + \overline{z_p}\,\Phi_p^{\infty\prime\prime} + \Psi_p^{\infty\prime}\right\} = -\mathrm{i}\tau_Y, \\
&\qquad\qquad\qquad\qquad\qquad\qquad\qquad\qquad\qquad\qquad \text{for} \quad 0 \leqslant u \leqslant l_p,
\end{aligned}\right\} \tag{3.11}$$

where

$$L(z, z_0; \alpha, \theta) = \Phi'_{\mathrm{R}} + \overline{\Phi'_{\mathrm{R}}} + \mathrm{e}^{2\mathrm{i}\theta}(\bar{z}\Phi''_{\mathrm{R}} + \Psi'_{\mathrm{R}}) - \frac{\alpha}{z+z_0} - \frac{\bar{\alpha}}{\bar{z}+\bar{z}_0} - \mathrm{e}^{2\mathrm{i}\theta}\left(-\frac{\bar{\alpha}}{z+z_0} - \frac{(\bar{z}+\bar{z}_0)\,\alpha}{(z+z_0)^2}\right). \tag{3.12}$$

The stress intensity factors K_{I} and K_{II} at the tips Q and Q′ of the tension cracks, and the shear mode stress intensity factor $K^{\mathrm{R}}_{\mathrm{II}}$ at the end R of the plastic zone, are given in terms of the values of α_{t} and α_{p} as follows:

$$\left.\begin{aligned} K_{\mathrm{I}} + \mathrm{i}K_{\mathrm{II}} &= \lim_{r \to l_{\mathrm{t}}} \; (2\pi)^{\frac{3}{2}}\, \mathrm{e}^{\mathrm{i}\theta}\, \overline{\alpha_{\mathrm{t}}(r)}\; (l_{\mathrm{t}} - r)^{\frac{1}{2}}, \\ \mathrm{i}K^{\mathrm{R}}_{\mathrm{II}} &= \lim_{t \to l_{\mathrm{p}}} \; (2\pi)^{\frac{3}{2}}\, \overline{\alpha_{\mathrm{p}}(t)}\; (l_{\mathrm{p}} - t)^{\frac{1}{2}}. \end{aligned}\right\} \tag{3.13}$$

From $(3.13)_2$, condition (3.2) requires

$$\lim_{t \to l_{\mathrm{p}}} \overline{\alpha_{\mathrm{p}}(t)}\; (l_{\mathrm{p}} - t)^{\frac{1}{2}} = 0. \tag{3.14}$$

Equations (3.11) with (3.10) form a system of integral equations for the dislocation densities α_{t} and α_{p}. Solving this system of integral equations subject to the condition (3.2), i.e. (3.14), we obtain the values of $K_{\mathrm{I}}/\tau_{\mathrm{Y}}(\pi c)^{\frac{1}{2}}$, $K_{\mathrm{II}}/\tau_{\mathrm{Y}}(\pi c)^{\frac{1}{2}}$ and $\sigma_1/\tau_{\mathrm{Y}}$ for assumed values of θ, l_{t} and l_{p} and given values of γ, σ_2/σ_1, μ and $\tau_{\mathrm{c}}/\tau_{\mathrm{Y}}$.

3.3. *Numerical results*

The basic parameters of the mathematical model are: the orientation of the flaw, γ; the size of the flaw, $2c$; the coefficient of friction, μ; the flaw cohesion, τ_{c}; the yield stress in shear, τ_{Y}, of the material that surrounds the flaw; and the corresponding fracture toughness, K_{c}. In the following, γ is taken to be 45°, placing the flaw in the maximum shear stress direction. It has been shown by Horii & Nemat-Nasser (1985*a*) that the friction and cohesion of the flaw produce similar effects, leading to essentially the same qualitative results; see their figure 5. For illustration, our numerical results are based on $\mu = 0.4$ and $\tau_{\mathrm{c}} = 0$. All calculations are made for proportional loading, by using various constant stress ratios, σ_2/σ_1. The stresses are normalized by using τ_{Y}, and the lengths are normalized by using half the flaw size, c.

The numerical calculations are made as follows:

1. For a given σ_2/σ_1, the normalized stress intensity factors, $K_{\mathrm{I}}/\tau_{\mathrm{Y}}(\pi c)^{\frac{1}{2}}$ and $K_{\mathrm{II}}/\tau_{\mathrm{Y}}(\pi c)^{\frac{1}{2}}$, and the normalized axial stress, $\sigma_1/\tau_{\mathrm{Y}}$, are calculated as functions of l_{p}/c, l_{t}/c and θ.

2. The orientation, θ, of the tension cracks, PQ and P′Q′ (figure 15), is chosen such that $K_{\mathrm{I}}/|\sigma_1|(\pi c)^{\frac{1}{2}}$ at Q and Q′ is maximized. (The critical value of θ is obtained for given values of l_{t}/c and l_{p}/c and a fixed value of σ_2/σ_1.) As a typical example, $K_{\mathrm{I}}/|\sigma_1|(\pi c)^{\frac{1}{2}}$ is plotted as a function of θ in figure 16 for $\sigma_2/\sigma_1 = 0$, $l_{\mathrm{p}}/c = 0.01$, 0.1 and 0.5, and indicated values of l_{t}/c (contours). The 'critical' value of θ corresponds to the peak of the associated curve in figure 16. This critical value is plotted in figure 17 as a function of l_{t}/c for $l_{\mathrm{p}}/c = 0.1$ and $\sigma_2/\sigma_1 = 0$, 0.1 and 0.2. It is seen that the critical θ is about 70° when tension cracks are initiated, and decreases with increasing crack length, approaching $\gamma = 45°$. As pointed out by Nemat-Nasser & Horii (1982), this implies that tension cracks initiate at the flaw tips at an angle of about 70° with respect to the flaw orientation, and then curve and grow toward the direction of maximum compression.

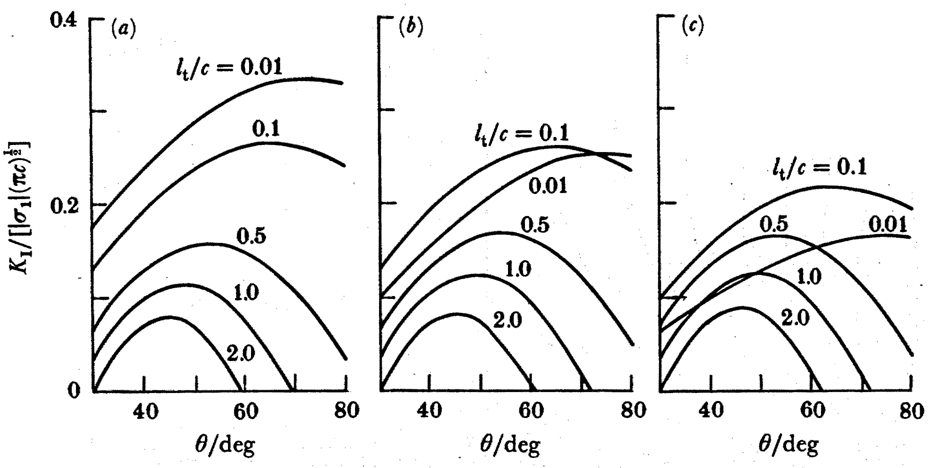

FIGURE 16. Normalized opening-mode stress intensity factor at the tips of tension cracks as a function of the crack orientation angle, for indicated crack lengths (contours of l_t/c) and plastic zone sizes: (*a*) $l_p/c = 0.01$; (*b*) $l_p/c = 0.1$; (*c*) $l_p/c = 0.5$.

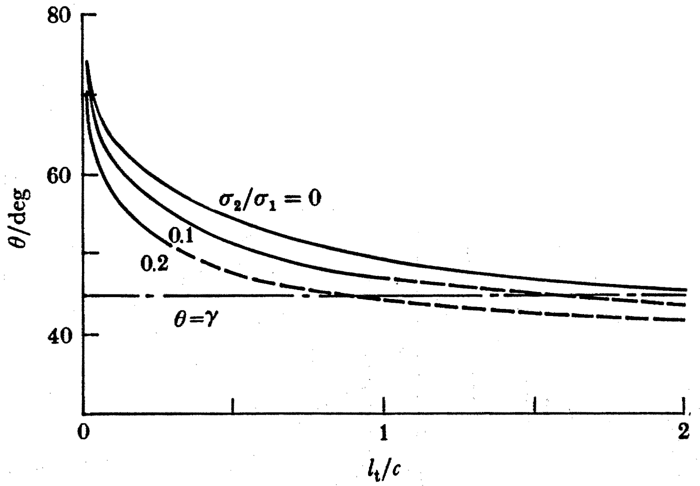

FIGURE 17. The optimal crack orientation angle as a function of the crack length for indicated stress ratios (contours of σ_2/σ_1); $\gamma = 45°$ and $l_p/c = 0.1$. Solid lines: $K_I > 0$; broken lines, $K_I < 0$.

3. For a fixed σ_2/σ_1 and given values of l_t/c and l_p/c, we obtain $K_I/\tau_Y(\pi c)^{\frac{1}{2}}$, $K_{II}/\tau_Y(\pi c)^{\frac{1}{2}}$ and σ_1/τ_Y corresponding to the critical θ. Typical results are shown in figures 18–22 for indicated values of σ_2/σ_1 where contours of constant (*a*) $K_I/\tau_Y(\pi c)^{\frac{1}{2}}$ and (*b*) $|\sigma_1|/\tau_Y$ are plotted in the l_t/c, l_p/c-plane.

4. From figures 18*a*–22*a*, for each σ_2/σ_1 we obtain a solution curve in the l_t/c, l_p/c-plane, by making use of the following criteria:

$$\left.\begin{array}{ll}\text{when tension cracks are growing,} & K_I = K_c,\\ \text{when tension cracks are stationary,} & 0 < K_I < K_c,\\ \text{and when tension cracks are closing,} & K_I = 0,\end{array}\right\} \tag{3.15}$$

where K_c is prescribed. The corresponding axial load $|\sigma_1|/\tau_Y$ is then established from data given

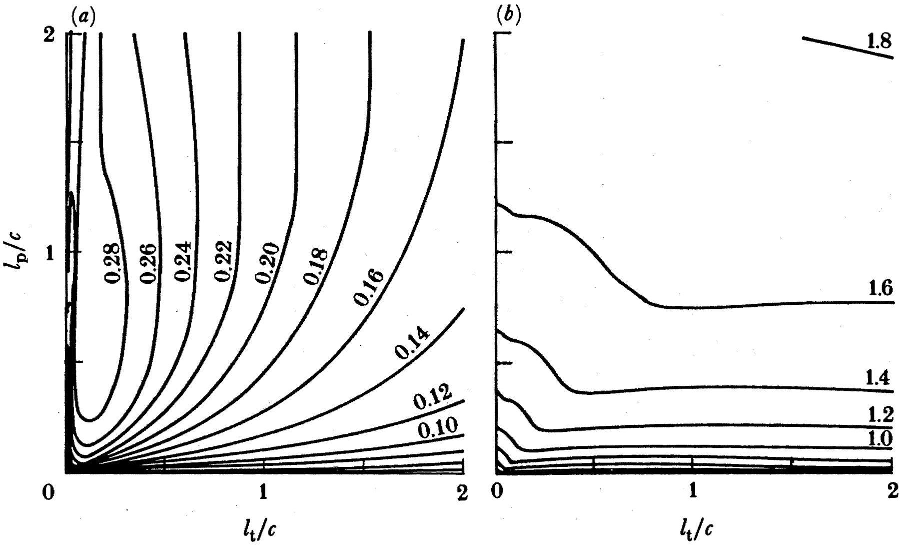

Figure 18. Contours of constant (*a*) $K_I/\tau_Y(\pi c)^{\frac{1}{2}}$ and (*b*) $|\sigma_1|/\tau_Y$ in the l_t, l_p-plane; $\sigma_2/\sigma_1 = 0$.

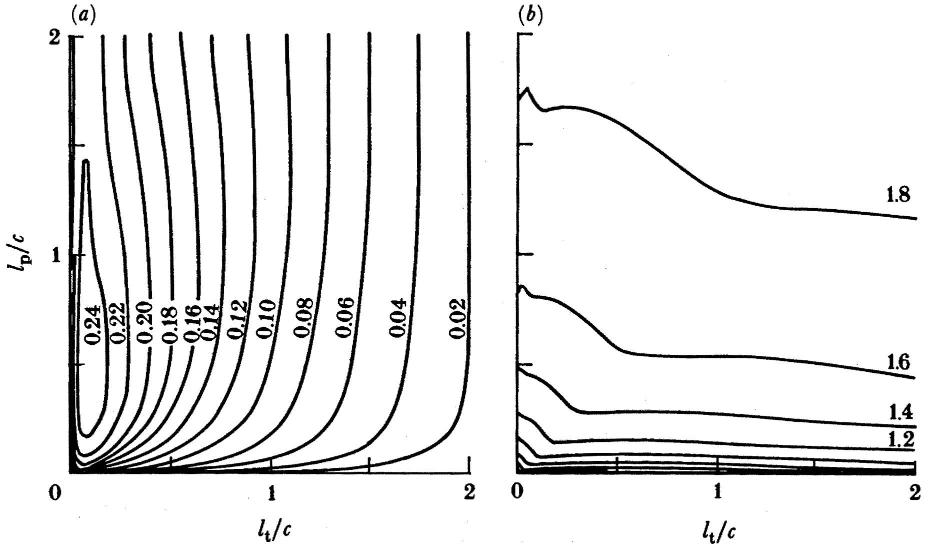

Figure 19. Contours of constant (*a*) $K_I/\tau_Y(\pi c)^{\frac{1}{2}}$ and (*b*) $|\sigma_1|/\tau_Y$ in the l_t, l_p-plane; $\sigma_2/\sigma_1 = 0.05$.

in figures 18*b*–22*b*. It is seen that different crack and plastic zone growth régimes are obtained for different values of the normalized fracture toughness

$$\Delta \equiv K_c/\tau_Y(\pi c)^{\frac{1}{2}}. \tag{3.16}$$

(Note that the normalized stress intensity factor is $K_I/\tau_Y(\pi c)^{\frac{1}{2}}$, with the fracture criteria given by (3.15).) We shall call Δ the 'ductility', whose value, as we shall see below, has a profound effect on the general response predicted by the model.

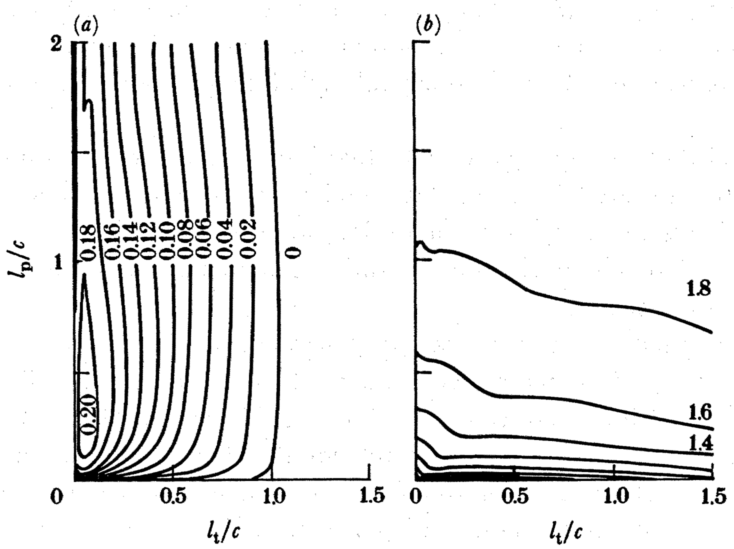

FIGURE 20. Contours of constant (*a*) $K_I/\tau_Y(\pi c)^{\frac{1}{2}}$ and (*b*) $|\sigma_1|/\tau_Y$ in the l_t, l_p-plane; $\sigma_2/\sigma_1 = 0.1$.

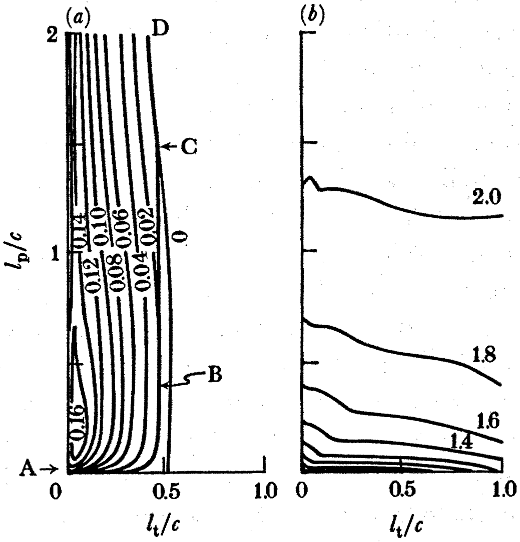

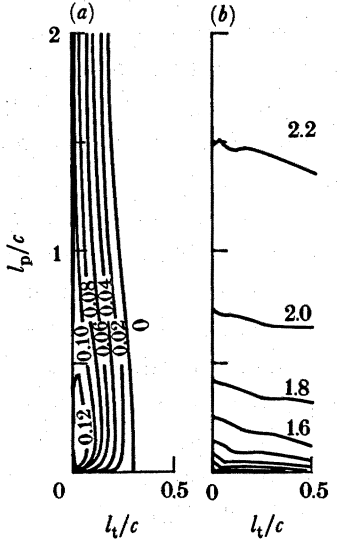

FIGURE 21. Contours of constant (*a*) $K_I/\tau_Y(\pi c)^{\frac{1}{2}}$ and (*b*) $|\sigma_1|/\tau_Y$ in the l_t, l_p-plane; $\sigma_2/\sigma_1 = 0.15$.

FIGURE 22. Contours of constant (*a*) $K_I/\tau_Y(\pi c)^{\frac{1}{2}}$ and (*b*) $|\sigma_1|/\tau_Y$ in the l_t, l_p-plane; $\sigma_2/\sigma_1 = 0.2$.

3.4. *Discussion of model results*

We shall now seek to explore the physical implications of our numerical results. We hasten to emphasize that all of these will be based on our mathematical model and therefore when we speak of, for example, a 'brittle or ductile response', it should be borne in mind that we mean a 'brittle or ductile response as predicted by our mathematical model'. As we shall show, however, it turns out that these predictions are in good accord with reported experimental observations.

There are essentially two quantities that characterize the model flaw: the coefficient of friction, μ, and the cohesion, τ_c/τ_Y. The values of these parameters affect the quantitative results, but they do not seem to alter in any substantial manner the qualitative nature of the model's physical implications. All the numerical calculations reported below are based on $\mu = 0.4$ and $\tau_c = 0$.

On the other hand there are two parameters that have a most profound influence on both the qualitative and quantitative character of the model's results: one parameter is the ductility, $\Delta = K_c/\tau_Y(\pi c)^{\frac{1}{2}}$, which is a measure of the material properties, and the other parameter is the stress ratio, σ_2/σ_1, which defines the loading condition and, in particular, the effect of confining pressure on the overall response.

Since with increasing temperature the fracture toughness, K_c, increases and the yield stress, τ_Y, decreases, the ductility, Δ, is an increasing function of temperature. It will be shown below that when Δ exceeds a critical value, say Δ_c (in our calculation, $\Delta_c = 0.26$), then plastic deformation dominates any possible microcracking, for all values of the stress ratio σ_2/σ_1. (Here and in what follows we restrict attention to the response under non-negative pressures, i.e. we do not consider the response under hydrostatic tension.) Values of Δ at room temperature for ductile metals, such as steel and aluminium, are relatively large (3 or 4 for steel and even greater for aluminium, when grain-size microflaws are assumed). For many crystalline rocks with grain-size microflaws, on the other hand, values of Δ are quite small at room temperature, being of the order of a few percent. These materials, therefore, are brittle at room temperature, although their response may be in a 'brittle mode' or a 'ductile mode', depending on the magnitude of the stress ratio σ_2/σ_1, as we shall discuss and illustrate in what follows.

An examination of the numerical results reveals three distinct modes for the growth régimes of tension cracks and plastic zones at the tips of the model flaw. When Δ and σ_2/σ_1 are suitably small, tension cracks initiate and grow to a finite length, and the size of the plastic zones is rather small. We shall refer to this as the 'brittle mode'. When, on the other hand, Δ or σ_2/σ_1, or both, are suitably large, plastic zones at the tips of the model flaw grow to a finite length before any cracking takes place. We shall refer to this as the 'ductile mode'. It turns out that the model predicts another mode, which we shall call the 'transitional mode', where first the plastic zones grow to a finite size before any cracking is initiated, but once the cracks are initiated they grow in an unstable manner to a finite length, and the length of the plastic zones decreases. The transitional mode occurs when the stress ratio is less than a threshold value, say R_c, and the ductility, Δ, is greater than a threshold value, say Δ_t, but still less than Δ_c. These and related concepts are discussed and illustrated below.

3.4.1. *Brittle mode*

In our calculation Δ_t turns out to be about 0.12. For ductility Δ less than this value and a stress ratio suitably small, the response is basically brittle, where, under an increasing axial load, the tension crack growth initially dominates the growth of the plastic zones.

As mentioned in the previous subsection, a relation between the crack length and the plastic zone size is established by using an appropriate figure from figures 18*a*–22*a* and the fracture criteria (3.15). A typical example is shown in figure 21*a* for $\sigma_2/\sigma_1 = 0.15$ and $\Delta = 0.02$. The curve starts at the origin; $l_t/c = 0$ and $l_p/c = 0$. As the axial load is increased, only the plastic zones develop, until the crack nucleation condition, $K_I = K_c$, is attained. This occurs at point A when $l_p/c = 0.002$, a negligibly small value. Upon further increase in axial stress at a constant stress ratio, both the tension cracks and the plastic zones grow monotonically, as indicated by the contour corresponding to $K_{\mathrm{I}}/\tau_{\mathrm{Y}}(\pi c)^{\frac{1}{2}} = \Delta = 0.02$, from A to B. At B the tension cracks attain their maximum size, after which, according to this model, the plastic zones continue to grow, relaxing the stress field at the crack tips and possibly causing partial crack closure. This occurs at point C, where the stress intensity factor, K_{I}, vanishes. From C to D the size of the 'open' portions of the tension cracks is reduced, so that the $K_{\mathrm{I}} = 0$ condition is maintained. We refer to this type of crack and plastic zone growth régime as the 'brittle mode', which is characterized by the initial part of the curve where tension crack growth dominates the plastic flow.

Similar results are obtained for other values of Δ and σ_2/σ_1 from figures 18*a*–22*a*. With the curve in the l_t/c, l_p/c-plane so established, the axial load can be calculated from figures 18*b*–22*b*. Figures 23 and 24 illustrate the crack and plastic zone growth régimes, and yield the relations between the axial load and the lengths of the crack and the plastic zone for $\Delta = 0.04$ and 0.08. It is seen that tension cracks cease to grow when the plastic zones attain a size comparable with the crack length. The growth of the plastic zones accelerates after the tension cracks attain their maximum length.

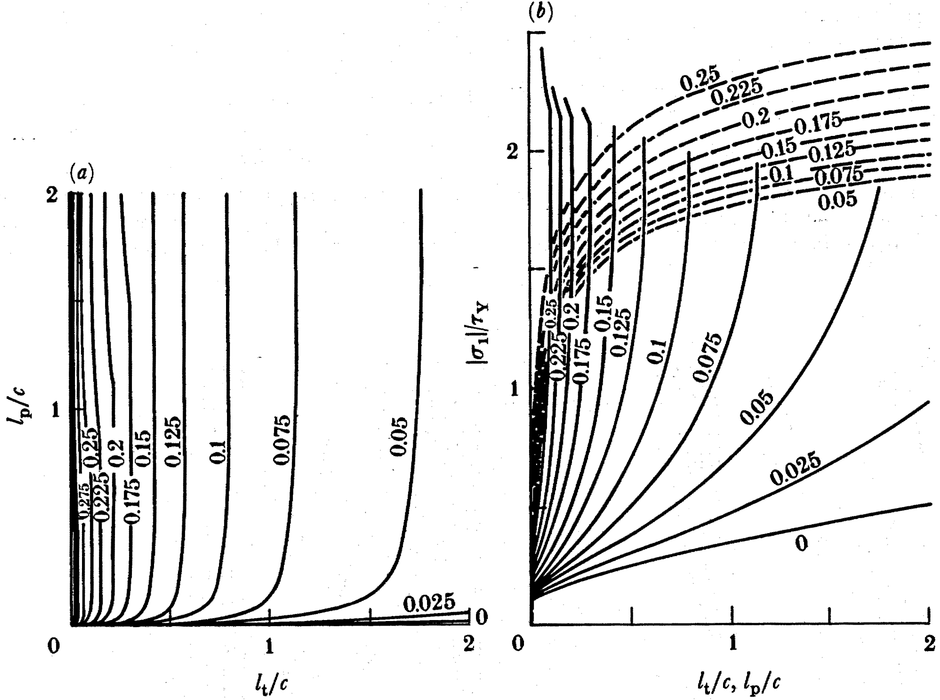

FIGURE 23. (*a*) Relation between the tension crack length and the size of the plastic zone under the proportional loading and indicated stress ratios (contours of σ_2/σ_1); (*b*) the corresponding relation between the axial load and the lengths of the tension crack (solid lines) and the plastic zone (broken lines). Ductility, $\Delta = 0.04$.

As discussed later, the maximum length of the tension cracks may be regarded as representing a measure of the underlying brittleness. This maximum length decreases with an increasing stress ratio, and eventually becomes negligibly small as the stress ratio is increased. At a certain stress ratio, the brittle mode changes to the ductile one, as discussed below.

3.4.2. *Ductile mode*

To examine the crack growth régime at very small crack lengths, contours of constant stress intensity factor, $K_{\mathrm{I}}/\tau_{\mathrm{Y}}(\pi c)^{\frac{1}{2}}$, are plotted in figure 25. (These figures are similar to those in figures 18*a*–22*a*, but with the l_t-axis magnified ten times.) From figure 25 and fracture criteria (3.15),

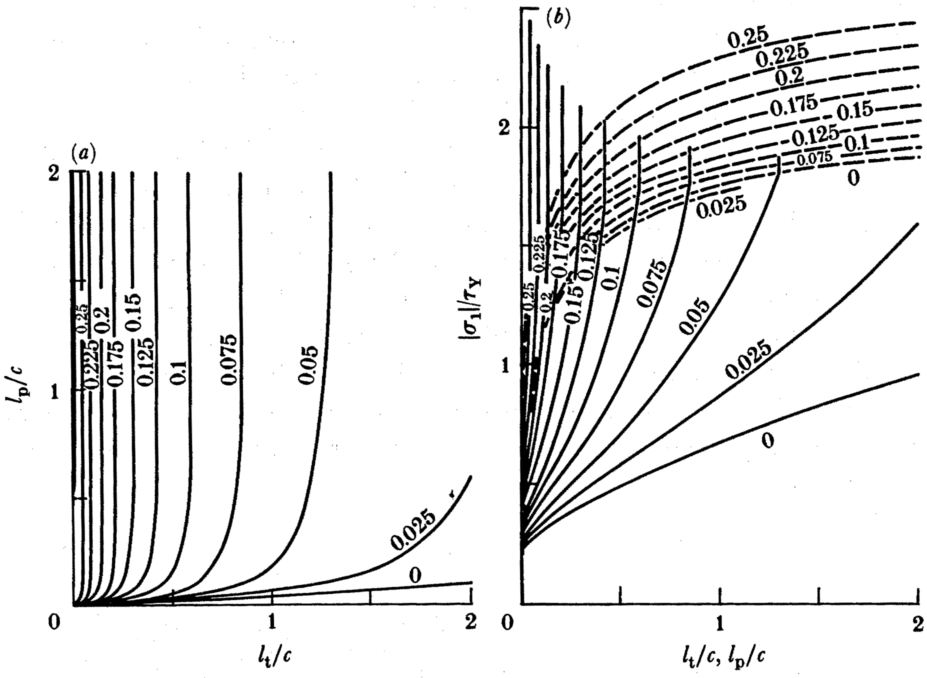

FIGURE 24. (*a*) Relation between the tension crack length and the size of the plastic zone under the proportional loading and indicated stress ratios (contours of σ_2/σ_1); (*b*) the corresponding relation between the axial load and the lengths of the tension crack (solid lines) and the plastic zone (broken lines). Ductility, $\Delta = 0.08$.

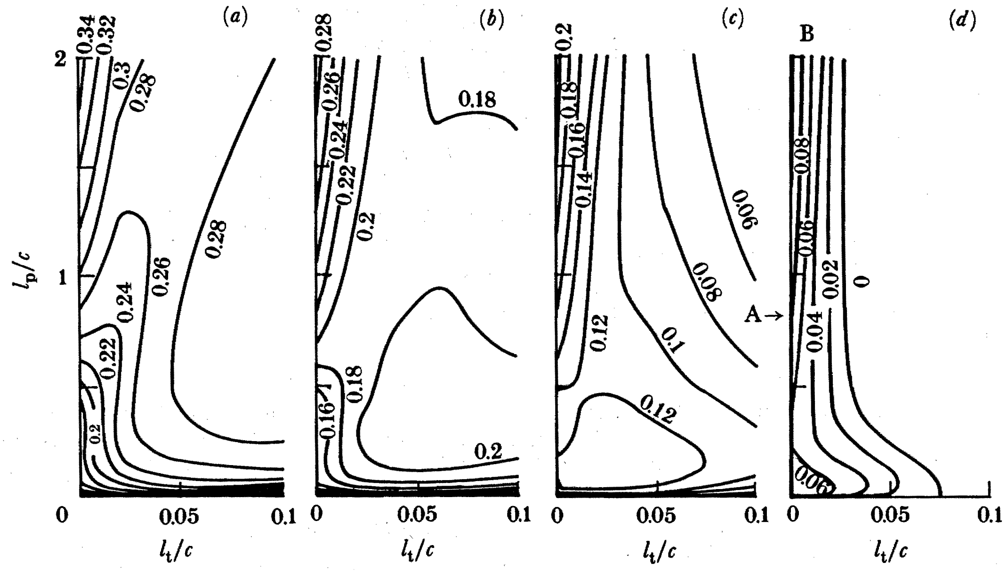

FIGURE 25. Contours of constant $K_I/\tau_Y(\pi c)^{\frac{1}{2}}$ in the l_t, l_p-plane, for stress ratios, σ_2/σ_1 of: (*a*) 0; (*b*) 0.1; (*c*) 0.2; (*d*) 0.3.

the crack and plastic zone growth régimes are obtained. Comparing with figure 21*a*, we observe a different pattern of crack and plastic zone growth in figure 25*d* for $\sigma_2/\sigma_1 = 0.3$ and $K_c/\tau_Y(\pi c)^{\frac{1}{2}} = 0.08$. Here the size of the plastic zones increases with increasing axial load, attaining a finite value, before cracks are initiated at point A. Even after crack initiation, the plastic zones continue to grow at a much faster rate than do the cracks, e.g. curve AB. A process of this kind characterizes the 'ductile mode'. The change from brittle to ductile mode is illustrated in figure 26*a*, *b* for $\Delta = 0.04$ and 0.08 respectively. It is seen that this change occurs when the stress ratio increases from 0.325 to 0.35 for $\Delta = 0.04$ and from 0.25 to 0.275 for $\Delta = 0.08$.

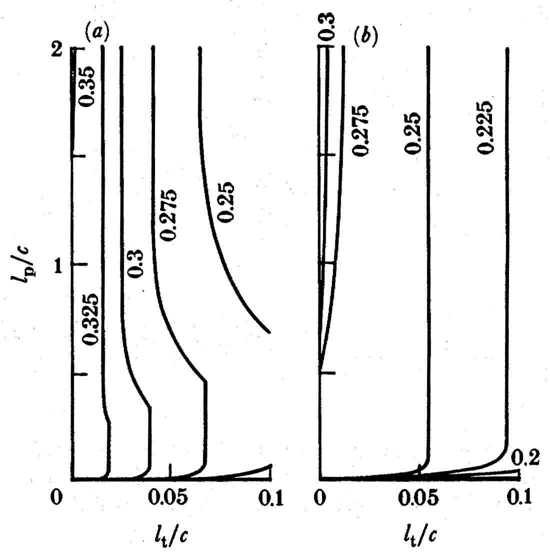

FIGURE 26. Relation between the tension crack length and the size of the plastic zone under proportional loading for indicated stress ratios (contours of σ_2/σ_1), for (*a*) $\Delta = 0.04$ and (*b*) $\Delta = 0.08$.

The threshold stress ratio, above which the response would be in the ductile mode, decreases as Δ increases (or as the temperature increases). It is seen from figure 25*a* that if Δ is greater than 0.26, the response is in the ductile mode even with zero stress ratio, i.e. under uniaxial compression.

3.4.3. *Transitional mode*

The numerical results show the existence of a threshold value for the ductility, denoted here by Δ_t (*ca.* 0.12), below which the growth of tension cracks and plastic zones is either in the brittle mode or in the ductile mode, as described above, depending on the stress ratio. In the brittle mode, the growth of cracks and plastic zones is stable, i.e. an increase in the axial load is required to increase the crack length and the plastic zone size (see figures 23*b* and 24*b*). On the other hand, if the ductility, Δ, is intermediate ($\Delta_t \approx 0.12 < \Delta < \Delta_c \approx 0.26$) and the stress ratio is small, we have a 'transitional mode', which is characterized by large plastic zones developing before crack initiation, and by unstable crack growth, accompanied by the shortening of plastic zones after crack initiation.

In the transitional mode the plastic zones first emerge and grow with increasing axial load until the condition for crack initiation is satisfied, i.e. until $K_I = K_c$. At this stage, tension cracks suddenly grow in an unstable manner, attaining a finite length, while the calculated size of the plastic zones decreases. (It is seen from figure 25 that with a relatively large Δ, the equilibrium curves $K_I/\tau_Y(\pi c)^{\frac{1}{2}} = \Delta$, following the initial plastic zone growth, show a decrease in plastic zone length l_p/c. The corresponding axial loads along these curves decrease and increase again, which results in an unstable crack growth.) Typical crack and plastic zone growth régimes are shown in figure 27 for $\Delta = 0.16$. Figure 27*b* displays a portion of figure

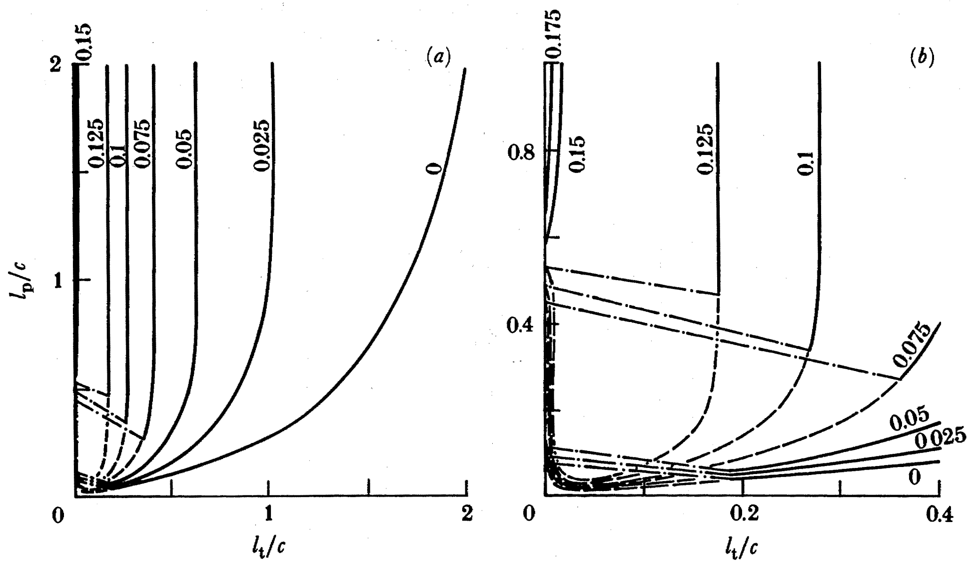

FIGURE 27. Relation between the tension crack length and the size of the plastic zone under proportional loading for indicated stress ratios (contours of σ_2/σ_1); solid curves for stable crack growth, dot–dashed lines for unstable crack growth, and broken curves for equilibrium states. Ductility, $\Delta = 0.16$.

27*a*, corresponding to small tension crack sizes. The solid and broken lines are equilibrium curves for indicated stress ratios; the solid lines are for stable growth. The dot-dashed lines indicate unstable crack growth accompanied by the shortening of plastic zone length. (Our calculations do not include the details of unloading with residual plastic strains.)

3.4.4. *Brittle–ductile transition*

From the results discussed above in this section, one may seek to quantify the brittle–ductile transition in terms of the variation of the material ductility, here identified by Δ, and the pressure, here presented by the stress ratio, σ_2/σ_1. The maximum length of the tension cracks represents a measure of the brittleness of the process. This maximum length is plotted as a function of σ_2/σ_1 for indicated Δ in figure 28. Solid lines correspond to the response in the brittle mode, and broken lines to the response in the transitional mode. The shaded area represents response in the ductile mode, where a maximum length for the tension cracks is not defined. All curves fall quickly with an increasing stress ratio, indicating the effect of pressure in suppressing brittleness. The maximum crack size at the same stress ratio decreases with increasing Δ. The transition from the brittle to the ductile mode occurs at lower stress ratios for larger values of Δ, indicating the influence of temperature in promoting ductile behaviour. The curve associated with $\Delta = 0$ displays the limit of brittleness. Even for this limiting case, the brittle response is seen to be suppressed at suitably large stress ratios.

3.4.5. *Brittle–ductile diagram*

It has been shown above that three different response modes are obtained depending on Δ and σ_2/σ_1. From results of figure 28 we may represent these schematically in a brittle–ductile diagram (see figure 29). (Note that these results are based on fixed $\mu (= 0.4)$ and $\tau_c (= 0)$ that characterize the properties of the flaw, and on a fixed flaw orientation, $\gamma (= 45°)$.) Curve ABC represents the threshold stress ratio above which the response would be in the ductile mode.

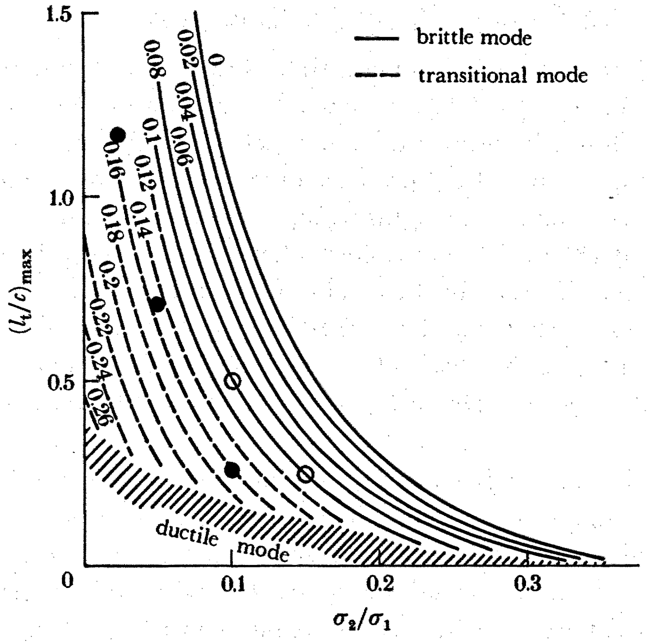

FIGURE 28. Maximum crack length as a function of the stress ratio for indicated ductilities (contours); circles are the results of model experiments (open, $c = 1.8$ cm; filled, $c = 0.9$ cm).

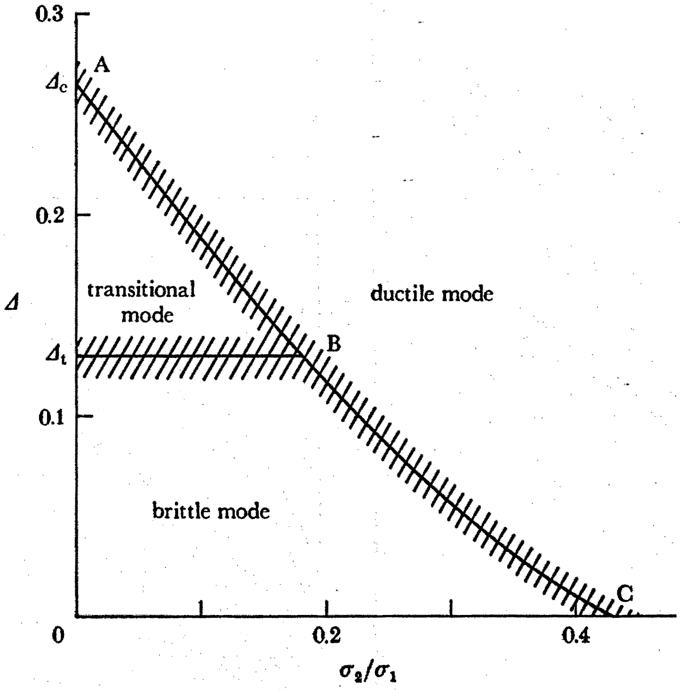

FIGURE 29. Brittle–ductile diagram.

The threshold stress ratio decreases as the ductility Δ increases. Below this curve, the response is in the brittle mode when Δ is less than $\Delta_t \approx 0.12$, and is in the transitional mode when Δ is greater than this. With the ductility greater than $\Delta_c \approx 0.26$, the response is in the ductile mode independently of the value of the stress ratio.

3.5. *Comparison with experimental results*

A series of model experiments on Columbia resin CR39 plates containing a single flaw is performed for $c = 9$ mm and $\sigma_2/\sigma_1 = 0.025$, 0.05 and 0.1, and for $c = 18$ mm and $\sigma_2/\sigma_1 = 0.1$ and 0.15; one of these is shown in figure 14. In all cases the tension cracks are arrested once they attain a finite length, because of the presence of lateral pressure (see figures 30 and 31, plate 5). The observed maximum crack lengths $(l_t/c)_{\max}$ are plotted in figure 28. It is seen that the data for $c = 9$ mm and 18 mm fall on the curves for $\Delta = 0.15$ and 0.1, respectively. From these results it follows that K_c/τ_Y for this material is about 0.8 mm$^{\frac{1}{2}}$; with this value, $\Delta = K_c/\tau_Y(\pi c)^{\frac{1}{2}} = 0.151$ for $c = 9$ mm and $\Delta = 0.106$ for $c = 18$ mm. It also should be pointed out that the observed crack growth is basically unstable for all the specimens with $c = 9$ mm, whereas it is stable for all the specimens with $c = 18$ mm. These observations agree well with our analytical results.

Experiments on actual rock samples have shown the response in triaxial compression to change from brittle to ductile as the confining pressure is increased. Mogi (1966) has summarized experimental data for different rocks (see figure 32). In these figures the ultimate strength of the specimen with brittle failure is marked with solid symbols. The stresses corresponding to the knee of the stress–strain curve are plotted with open and semi-solid symbols

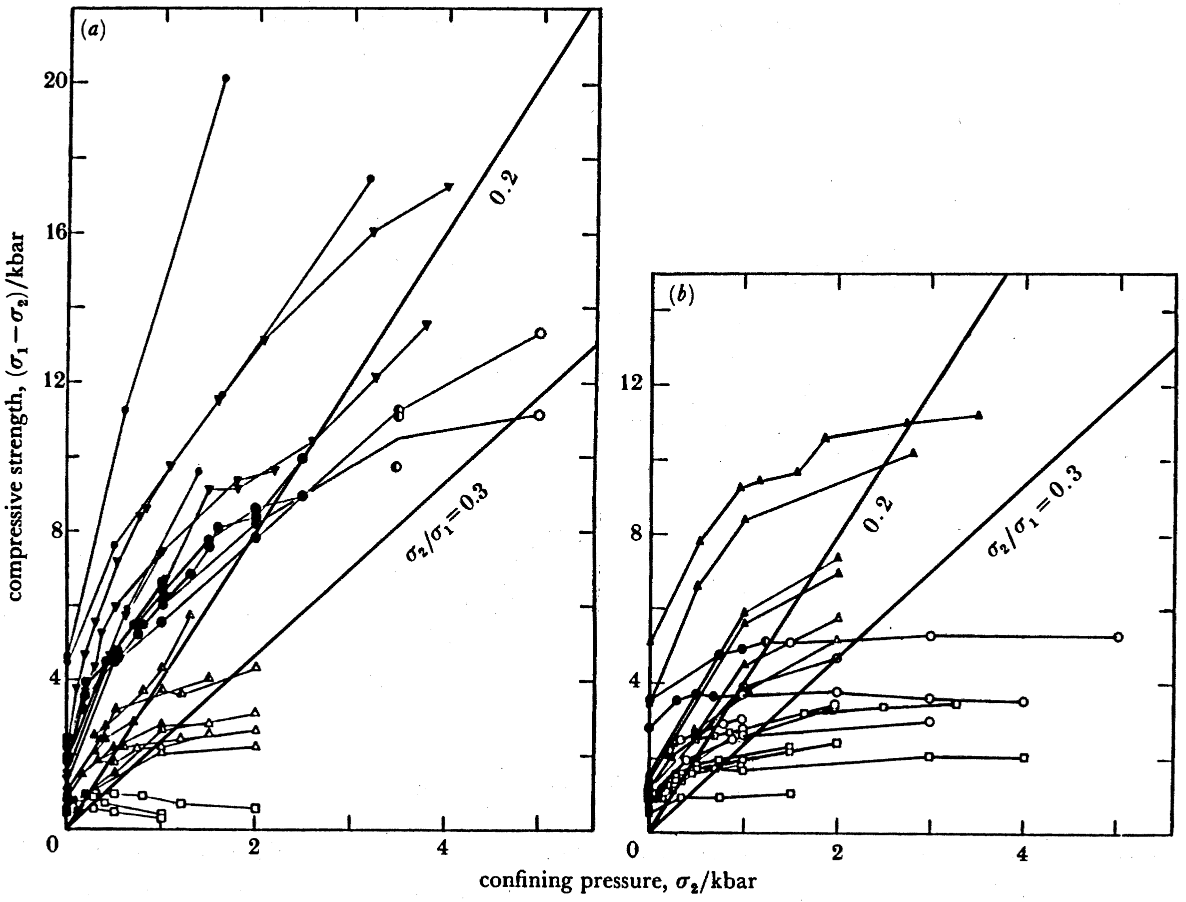

FIGURE 32. Variation of compressive strength with confining pressure for (*a*) silicate rocks and (*b*) carbonate rocks. (From Mogi (1966).)

for the ductile response and the transitional response, respectively. It is seen that an increase in the stress ratio from 0.2 to 0.3 results in a change from brittle failure to ductile deformation. Our analytical results (figure 28) are in accord with this interesting feature. According to our model, the maximum crack length – a measure of the brittleness of the process – decreases dramatically with increasing stress ratio, and when this ratio changes from 0.2 to 0.3, the size of the tension cracks becomes negligibly small.

Figure 33*a*, plate 6, shows two collinear flaws. The plate is compressed, keeping $\sigma_2/\sigma_1 = 0.05$. Figure 33*b* shows arrested tension cracks at the tips of the flaws. Figure 33*c* is the photoelastic picture showing the residual strains due to the plastic deformation in the *unloaded* specimen. The maximum plastic deformation takes place between the pre-existing flaws. In the actual rock specimen, the effects of the interaction between adjacent cracks and adjacent plastic zones are considered to be important to the brittle–ductile transition process. However, the proposed model seems to capture certain fundamental features observed experimentally, even though it does not include these interaction effects.

3.6. *Analytic estimate*

The solution of integral equations (3.10) and (3.11) requires rather involved numerical calculations. In certain applications a simple closed-form analytic estimate, albeit approximate, may prove more useful. In this section we present such an approximate solution, and using the exact results, show that the solution yields reasonable results for responses in the brittle mode, i.e. when ductility is about 0.1 or less.

An examination of figure 25 reveals a rather complex relation between the length of the tension cracks and that of the plastic zones when these quantities are small and when the ductility exceeds Δ_t. On the other hand, when the ductility is suitably small and the size of the tension cracks is suitably large relative to the size of the plastic zones, the interaction effects between the cracks and the plastic zones seem to be less important. Therefore, for this range of response, one may seek to estimate the stress intensity factor K_{I} at the crack tips Q and Q′ in figure 15 and the corresponding axial load, in terms of l_t/c, l_p/c and σ_2/σ_1, by completely ignoring the interaction effects.

To this end, one may estimate K_{I} at the crack tips from (2.6), which does not involve the size of the plastic zones. Then one may use the Dugdale model (Dugdale 1960) in mode II to estimate the axial stress corresponding to the plastic zone size, such that $K_{\mathrm{II}}^{\mathrm{R}}$ vanishes at points R and R′ in figure 15. As shown in figure 34, one may consider a mode II crack with the boundary condition

$$\left.\begin{aligned} \tau_{xy} &= -\tau_{xy}^{\infty}-\tau_{\mathrm{c}}+\mu\sigma_y^{\infty}, \quad \text{on} \quad |x|<c,\\ \tau_{xy} &= -\tau_{xy}^{\infty}-\tau_{\mathrm{Y}}, \quad \text{on} \quad c<|x|<c+l_{\mathrm{p}}.\end{aligned}\right\} \tag{3.17}$$

Since the stress intensity factor is given by

$$K_{\mathrm{II}} = (-\tau_{xy}^{\infty}-\tau_{\mathrm{c}}+\mu\sigma_y^{\infty})\,[\pi(c+l_{\mathrm{p}})]^{\frac{1}{2}}+\frac{\tau_{\mathrm{c}}-\mu\sigma_y^{\infty}-\tau_{\mathrm{Y}}}{[\pi(c+l_{\mathrm{p}})]^{\frac{1}{2}}}\,2(c+l_{\mathrm{p}})\left[\tfrac{1}{2}\pi-\arcsin\left(\frac{1}{1+l_{\mathrm{p}}/c}\right)\right], \tag{3.18}$$

the condition (3.2) yields

$$l_{\mathrm{p}}/c = \operatorname{cosec}\frac{\pi(-\tau_{xy}^{\infty}-\tau_{\mathrm{Y}})}{2(\tau_{\mathrm{c}}-\mu\sigma_y^{\infty}-\tau_{\mathrm{Y}})}-1. \tag{3.19}$$

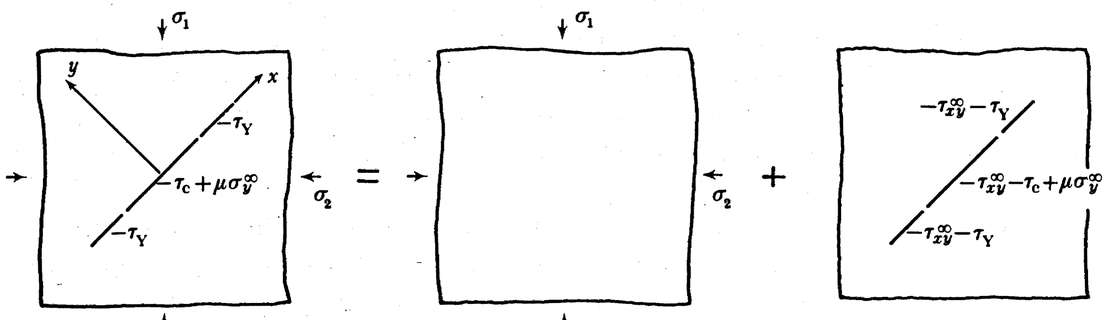

FIGURE 34

Substitution for τ_{xy}^∞ and some manipulation then result in

$$(-\sigma_1)/\tau_Y=\left[2+\frac{4}{\pi}(\tau_c/\tau_Y-1)\arcsin\left(\frac{1}{1+l_p/c}\right)\right]\Big/$$
$$\left\{(1-\sigma_2/\sigma_1)\sin 2\gamma-\mu[1+\sigma_2/\sigma_1-(1-\sigma_2/\sigma_1)\cos 2\gamma]\frac{2}{\pi}\arcsin\left(\frac{1}{1+l_p/c}\right)\right\}. \tag{3.20}$$

We now propose to use $(2.6)_1$ and (3.20) for calculating $K_I/\tau_Y(\pi c)^{\frac{1}{2}}$ and σ_1/σ_Y. Indeed, from (2.6) one easily obtains the expression

$$\frac{K_I}{\tau_Y(\pi c)^{\frac{1}{2}}}=\frac{\sin\theta}{\pi(l_t/c+l_t^*/c)^{\frac{1}{2}}}\left\{\frac{(-\sigma_1)}{\tau_Y}[(1-\sigma_2/\sigma_1)\sin 2\gamma-\mu(1+\sigma_2/\sigma_1-(1-\sigma_2/\sigma_1)\cos 2\gamma)]-\frac{\tau_c}{\tau_Y}\right\}$$
$$-(l_t/c)^{\frac{1}{2}}\frac{(-\sigma_1)}{\tau_Y}\tfrac{1}{2}[1+\sigma_2/\sigma_1-(1-\sigma_2/\sigma_1)\cos 2(\theta-\gamma)], \tag{3.21}$$

where $(-\sigma_1)/\tau_Y$ is given by (3.20).

It remains to show the accuracy of these estimates. To this end, we have plotted in figure 35 the estimated relations between l_t/c and l_p/c by broken lines, together with the numerical results of the exact formulation, by solid lines. It is seen that for ductility less than or equal

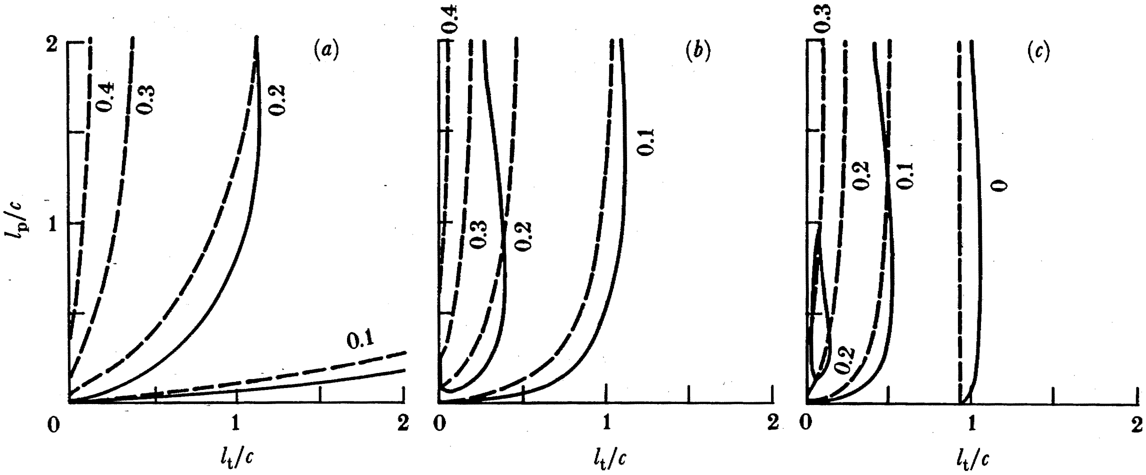

FIGURE 35. Contours of constant $K_I/\tau_Y(\pi c)^{\frac{1}{2}}$ in the l_t, l_p-plane for indicated stress ratios, σ_2/σ_1: (a) 0; (b) 0.05; (c) 0.1. Solid curves are from the exact (numerical) calculation and broken curves are from the analytic estimate (3.21).

to 0.1, the estimates are reasonably accurate, especially in the range of loading before the formation of large plastic zones. However, the approximate estimate for the response in the brittle mode does not yield a maximum value for the size of the tension cracks, whereas the exact calculation does. Referring to the exact results displayed in figures 18–27, note that the maximum size of the tension cracks is attained at a stage where the size of the plastic zones is almost the same as that of the tension cracks. With this information in mind, we define for the approximate solution the measure of brittleness to be the size of the tension cracks when $l_p = l_t$. In figure 36 we have plotted this measure of brittleness as a function of the stress ratio

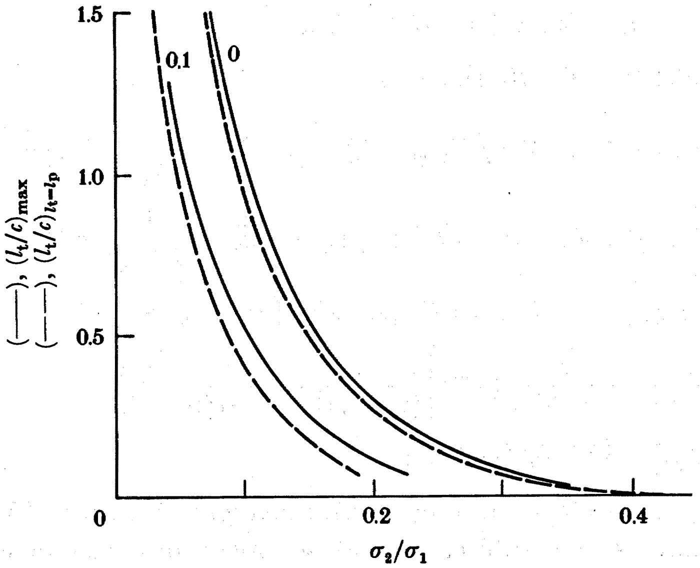

FIGURE 36. Maximum crack length as a function of stress ratio for indicated ductility, Δ: solid curves are from the exact (numerical) calculation, and broken curves are from the analytic estimates (2.6) and (3.21) for $l_t = l_p$.

and the ductility, together with the curves corresponding to the maximum size of the tension cracks taken from figure 28. It is seen that the approximate results are quite good estimates for ductility less than 0.1.

This work was supported by the U.S. Air Force Office of Scientific Research under grant no. AFOSR-84-0004 to Northwestern University and grant no. AFOSR-86-0035 to the University of California, San Diego.

APPENDIX A

With reference to figure 1, let the common length of the curved cracks PQ and P′Q′ be l, and the profile of PQ be defined by $x = c+g(r)$ and $y = f(r)$, where r measures length along PQ. The required stress potentials are given by (3.6). Hence, considering dislocations of density $\alpha(r)$, suitably distributed on PQ and P′Q′, from (2.2) and (3.8) we obtain

$$\int_0^l [\Phi^{D\prime}+\overline{\Phi^{D\prime}}+e^{2i\theta}(\bar{z}\Phi^{D\prime\prime}+\Psi^{D\prime})]\,dr+\Phi^{\infty\prime}+\overline{\Phi^{\infty\prime}}+e^{2i\theta}(\bar{z}\Phi^{\infty\prime\prime}+\Psi^{\infty\prime}) = 0, \qquad (A\,1)$$

with

$$z_0 = c+g(r)+if(r), \quad z = c+g(s)+if(s), \quad \alpha = \alpha(r), \quad \theta = \tan^{-1}[f'(s)/g'(s)]. \qquad (A\,2)$$

The first condition of (2.1) requires

$$\int_0^l [\alpha(r)+\overline{\alpha(r)}]\,\mathrm{d}r = 0. \tag{A 3}$$

Equation (A 1) can be rewritten as

$$\int_0^l \frac{\alpha M_1+\bar{\alpha} M_2}{s-r}\,\mathrm{d}r+\int_0^l [\alpha L_1+\bar{\alpha} L_2]\,\mathrm{d}r+(\tau_{xy}^{\infty}-\mu\sigma_y^{\infty}+\tau_{\mathrm{c}})\,S+\sigma_{\theta}^{\infty}+\mathrm{i}\tau_{r\theta}^{\infty}=0, \tag{A 4}$$

where

$$\left.\begin{aligned}
M_1(r,s) &= 1/h-\mathrm{e}^{2\mathrm{i}\theta}\,\bar{h}/h^2, \quad M_2(r,s) = 1/\bar{h}+\mathrm{e}^{2\mathrm{i}\theta}/h,\\
h(r,s) &= [g(s)-g(r)+\mathrm{i}(f(s)-f(r))]/(s-r),\\
L_1(r,z,\theta) &= \beta U\{F(z,z_0)+F(z,\overline{z_0})\}+\bar{\beta}U\{(z_0-\overline{z_0})\,G(z,z_0)\}-\frac{1}{z+z_0}+\mathrm{e}^{2\mathrm{i}\theta}\frac{\bar{z}+\overline{z_0}}{(z+z_0)^2},\\
L_2(r,z,\theta) &= -\bar{\beta}U\{F(z,z_0)+F(z,\overline{z_0})\}-\beta U\{(\overline{z_0}-z_0)\,G(z,\overline{\overline{z_0}})\}-\frac{1}{\bar{z}+\overline{z_0}}+\mathrm{e}^{2\mathrm{i}\theta}\frac{1}{z+z_0},\\
U\{F(z,z_0)\} &= U\{\theta;F(z,z_0)\} = -F(z,z_0)+F(\bar{z},z_0)+\mathrm{e}^{2\mathrm{i}\theta}[2F(z,z_0)+(z-\bar{z})\,F'(z,z_0)],\\
S(z,\theta) &= \tfrac{1}{2}\mathrm{i}\left\{\frac{\bar{z}}{(\bar{z}^2-c^2)^{\frac{1}{2}}}-\frac{z}{(z^2-c^2)^{\frac{1}{2}}}+\mathrm{e}^{2\mathrm{i}\theta}\left[\frac{(\bar{z}-z)c^2}{(z^2-z_0^2)^{\frac{3}{2}}}+\frac{2z}{(z^2-c^2)^{\frac{1}{2}}}-2\right]\right\},\\
\sigma_{\theta}^{\infty}+\mathrm{i}\tau_{r\theta}^{\infty} &= \Phi_0^{\infty\prime}+\overline{\Phi_0^{\infty\prime}}+\mathrm{e}^{2\mathrm{i}\theta}\,(\bar{z}\Phi_0^{\infty\prime\prime}+\Psi_0^{\infty\prime}),
\end{aligned}\right\} \tag{A 5}$$

with $z = z(s)$, $z_0 = z_0(r)$ and $\theta = \theta(s)$ given by (A 2). Equations (A 4), with (A 3), define the dislocation density α. Solving (A 4) subject to (A 3), we obtain the stress intensity factors at the tips, Q and Q′, of the curved cracks PQ and P′Q′ from

$$K_{\mathrm{I}}+\mathrm{i}K_{\mathrm{II}} = \lim_{r\to l}\tfrac{1}{2}(2\pi)^{\frac{3}{2}}\,(l-r)^{\frac{1}{2}}\,[\alpha(r)\,M_1(r,l)+\overline{\alpha(r)}\,M_2(r,l)]. \tag{A 6}$$

When PQ and P′Q′ are straight lines, we obtain

$$M_1 = 0,\ M_2 = 2\mathrm{e}^{2\mathrm{i}\theta},\ \theta(s) = \theta = \text{const.},\ z = c+s\mathrm{e}^{\mathrm{i}\theta},\ \text{and}\ z_0 = c+r\mathrm{e}^{\mathrm{i}\theta}. \tag{A 7}$$

In this case the formulation becomes identical with that of Nemat-Nasser & Horii (1982), except for $F(z,z_0)$ and $G(z,z_0)$, which are given by (3.7) (see Nemat-Nasser 1983; Horii & Nemat-Nasser 1983, 1985*a*).

For curved crack extensions, with given crack profile, $f(r)$ and $g(r)$, the singular integral equation (A 4), subject to the constraint (A 3), is solved by using the numerical method of Gerasoulis & Srivastav (1981). The crack profile is obtained incrementally where we consider a sequence of incremental straight extensions, each with an orientation that maximizes the opening-mode stress intensity factor, K_{I}, at the extended crack tip.

Nemat-Nasser & Horii (1982) suggest an approximate scheme for calculating the crack profile, on the basis of the results of the *straight* crack extension calculations; see their equations (21) and the corresponding discussion. Horii & Nemat-Nasser (1985*a*) show that the straight crack extension model is in good accord with the more complete curved crack extension solution, and, for the sake of simplicity in calculation, they use this model in their analysis of faulting.

The method of pseudo-tractions requires an explicit solution of the singular integral equation (A 4). This integral equation can, of course, be solved as accurately as desired. However, for application to the analysis of unstable growth of cracks emanating from the tips of a row of pre-existing flaws, the stress intensity factor and other parameters must be calculated repeatedly for various values of confining pressure, individual flaw orientation, and other relevant parameters. To simplify this procedure, Horii & Nemat-Nasser (1985*a*) introduce the following approximate method for the solution of (A 4), which seems to yield adequately accurate results.

First, the distribution of the dislocation density is approximated by

$$\alpha(r) = \{1/[r(l-r)]^{\frac{1}{2}}\}\,[\eta^{\mathrm{R}}(2r/l-1)+\mathrm{i}\eta^{\mathrm{I}}r/l], \tag{A 8}$$

which satisfies (A 3), where η^{R} and η^{I} are two real unknown parameters to be determined. Then the integrand of the second term in (A 4) is estimated by

$$\begin{aligned}\alpha(r)\,L_1(r,z,\theta)+\overline{\alpha(r)}\,L_2(r,z,\theta) = \{1/[r(l-r)]^{\frac{1}{2}}\}\{[(\eta^{\mathrm{R}}+\mathrm{i}\eta^{\mathrm{I}})\,L_1(l,z,\theta)\\ +(\eta^{\mathrm{R}}-\mathrm{i}\eta^{\mathrm{I}})\,L_2(l,z,\theta)]\,r/l-\eta^{\mathrm{I}}[L_1(0,z,\theta)+L_2(0,z,\theta)]\,(1-r/l)\}.\end{aligned} \tag{A 9}$$

The integral equation (A 4) now becomes

$$\begin{bmatrix} A_1 & A_2 \\ A_3 & A_4 \end{bmatrix}\begin{bmatrix}\eta^{\mathrm{R}} \\ \eta^{\mathrm{I}}\end{bmatrix} = \begin{bmatrix}(\tau_{xy}^{\infty}-\mu\sigma_y^{\infty}+\tau_{\mathrm{c}})\ \mathrm{Re}\,[S]+\sigma_{\theta}^{\infty} \\ (\tau_{xy}^{\infty}-\mu\sigma_y^{\infty}+\tau_{\mathrm{c}})\ \mathrm{Im}\,[S]+\tau_{r\theta}^{\infty}\end{bmatrix}, \tag{A 10}$$

where

$$\left.\begin{aligned}A_1+\mathrm{i}A_3 &= \tfrac{1}{2}\pi[(8/l)\mathrm{e}^{\mathrm{i}\theta}-L_1(l,z,\theta)-L_2(l,z,\theta)+L_1(0,z,\theta)+L_2(0,z,\theta)],\\ -A_4+\mathrm{i}A_2 &= \tfrac{1}{2}\pi[(4/l)\mathrm{e}^{\mathrm{i}\theta}+L_1(l,z,\theta)+L_2(l,z,\theta)].\end{aligned}\right\} \tag{A 11}$$

Since *s* may be suitably chosen, for convenience the following expressions are used:

$$s/l = \left.\begin{cases} -0.075(l/c)+0.475, & \text{for}\quad l/c<1,\\ -0.0074(l/c)^3+0.0156(l/c)^2-0.104(l/c)+0.489, & \text{for}\quad 1<l/c<4,\\ -0.015(l/c)+0.335, & \text{for}\quad 4<l/c.\end{cases}\right\} \tag{A 12}$$

From (A 6–A 8), we finally have

$$K_{\mathrm{I}}+\mathrm{i}K_{\mathrm{II}} = (2\pi)^{\frac{3}{2}}\,\mathrm{e}^{\mathrm{i}\theta}(\eta^{\mathrm{R}}-\mathrm{i}\eta^{\mathrm{I}})/l^{\frac{1}{2}}. \tag{A 13}$$

Equations (A 10) are solved for η^{R} and η^{I}, and the stress intensity factors at the tips of straight crack extensions are obtained from (A 13). Adopting the fracture criterion that the most favourable orientation of the crack extension results in the maximum K_{I}, we calculate the crack orientation angle, θ.

Horii & Nemat-Nasser (1985*a*) compare the results of this approximate solution with those of the exact analysis, arriving at a reasonably good correlation; see their figure A 5.

APPENDIX B

The elasticity problem to be solved is shown in figure 8; see §2.3. It is solved by making use of the method of pseudo-tractions (Horii & Nemat-Nasser 1985*b*). In this method, the solution to the original problem is obtained by the superposition of the solutions of a number of sub-problems and the uniform far-field stresses. Each sub-problem involves an infinite homogeneous solid containing only one of the flaws and its associated cracks. For each sub-problem, the boundary conditions along the typical pre-existing flaw PP′ are

$$u_y^+ = u_y^-, \quad \tau_{xy} + \tau_{xy}^{\mathrm{P}} + \tau_{xy}^{\infty} = -\tau_{\mathrm{c}} + \mu(\sigma_y + \sigma_y^{\mathrm{P}} + \sigma_y^{\infty}), \tag{B 1}$$

and along the corresponding cracks PQ and P′Q′,

$$\sigma_\theta + \sigma_\theta^{\mathrm{P}} + \sigma_\theta^{\infty} = 0, \quad \tau_{r\theta} + \tau_{r\theta}^{\mathrm{P}} + \tau_{r\theta}^{\infty} = 0. \tag{B 2}$$

The quantities σ_y^{P}, τ_{xy}^{P}, $\sigma_\theta^{\mathrm{P}}$ and $\tau_{r\theta}^{\mathrm{P}}$ are called the 'pseudo-tractions'. They are the unknown functions that must be determined in such a manner as to satisfy all boundary conditions of the original problem. The requirement that the superposition of the sub-problems must be equivalent to the original problem leads to a system of integral equations for these pseudo-tractions. These equations are the 'consistency conditions'. By making the unknown pseudo-tractions discrete, the system of integral equations is reduced to a system of algebraic equations. Because of symmetry, the pseudo-tractions are the same for all inhomogeneities. For simplicity we approximate the pseudo-tractions by piecewise constant functions, i.e. we assume that σ_y^{P} and τ_{xy}^{P} are constants along PP′, and $\sigma_\theta^{\mathrm{P}}$ and $\tau_{r\theta}^{\mathrm{P}}$ are constants along PQ and P′Q′.

Following the approximate method proposed in Appendix A, the solution of a typical sub-problem is given by

$$\begin{bmatrix} A_1 & A_2 \\ A_3 & A_4 \end{bmatrix} \begin{bmatrix} \eta^{\mathrm{R}} \\ \eta^{\mathrm{I}} \end{bmatrix} = \begin{bmatrix} [\tau_{xy}^{\infty} + \tau_{xy}^{\mathrm{P}} - \mu(\sigma_y^{\infty} + \sigma_y^{\mathrm{P}}) + \tau_{\mathrm{c}}]\, \mathrm{Re}\,[S] + \sigma_\theta^{\infty} + \sigma_\theta^{\mathrm{P}} \\ [\tau_{xy}^{\infty} + \tau_{xy}^{\mathrm{P}} - \mu(\sigma_y^{\infty} + \sigma_y^{\mathrm{P}}) + \tau_{\mathrm{c}}]\, \mathrm{Im}\,[S] + \tau_{r\theta}^{\infty} + \tau_{r\theta}^{\mathrm{P}} \end{bmatrix}, \tag{B 3}$$

where S is given in (A 5), and the A are given in (A 11).

The normal and shear tractions, σ_ψ and $\tau_{\rho\psi}$, acting at a point z on a plane inclined from the x-direction by the angle ψ, are given by

$$\sigma_\psi + \mathrm{i}\tau_{\rho\psi} = B_1(z,\psi)\,\eta^{\mathrm{R}} + B_2(z,\psi)\,\eta^{\mathrm{I}} + [\tau_{xy}^{\infty} + \tau_{xy}^{\mathrm{P}} - \mu(\sigma_y^{\infty} + \sigma_y^{\mathrm{P}}) + \tau_{\mathrm{c}}]\, S(z,\psi), \tag{B 4}$$

where

$$\left.\begin{aligned} B_1(z,\psi) &= 2\mathrm{Re}\,[2I_1 - I_2] + \mathrm{e}^{2\mathrm{i}\psi}\,(2I_1 - I_2 + 2II_1 - II_2) \\ &\quad + \tfrac{1}{2}\pi[L_1(l,z,\psi) + L_2(l,z,\psi) - L_1(0,z,\psi) - L_2(0,z,\psi)], \\ B_2(z,\psi) &= -2\mathrm{Im}\,[I_1] + \mathrm{i}\,\mathrm{e}^{2\mathrm{i}\psi}(-I_1 + II_1) + \tfrac{1}{2}\mathrm{i}\pi[L_1(l,z,\psi) - L_2(l,z,\psi)], \end{aligned}\right\} \tag{B 5}$$

with

$$\left.\begin{aligned} I_1 &= \frac{1}{l}\int_0^l \frac{r\,\mathrm{d}r}{[r(l-r)]^{\frac{1}{2}}\,(z-c-r\,\mathrm{e}^{\mathrm{i}\theta})} = \frac{\mathrm{e}^{-\mathrm{i}\theta}}{l}\pi\left\{\frac{z-c}{[(z-c)\,(z-z_{\mathrm{t}})]^{\frac{1}{2}}} - 1\right\}, \\ I_2 &= \int_0^l \frac{\mathrm{d}r}{[r(l-r)]^{\frac{1}{2}}\,(z-c-r\,\mathrm{e}^{\mathrm{i}\theta})} = \frac{\pi}{[(z-c)\,(z-z_{\mathrm{t}})]^{\frac{1}{2}}}, \\ II_1 &= -\frac{1}{l}\int_0^l \frac{r(z-c-r\,\mathrm{e}^{-\mathrm{i}\theta})\,\mathrm{d}r}{[r(l-r)]^{\frac{1}{2}}\,(z-c-r\,\mathrm{e}^{\mathrm{i}\theta})^2} \\ &= -\frac{\mathrm{e}^{-3\mathrm{i}\theta}}{l}\pi\left\{\frac{(z-c)\,[(z-c)\,(3z-3z_{\mathrm{t}}-z+c) + (z-c)\,(z_{\mathrm{t}}-c)\,\mathrm{e}^{2\mathrm{i}\theta}}{2[(z-c)\,(z-z_{\mathrm{t}})]^{\frac{3}{2}}} - 1\right\}, \\ II_2 &= -\int_0^l \frac{(z-c-r\,\mathrm{e}^{-\mathrm{i}\theta})\,\mathrm{d}r}{[r(l-r)]^{\frac{1}{2}}\,(z-c-r\,\mathrm{e}^{\mathrm{i}\theta})^2} \\ &= \frac{\mathrm{e}^{-2\mathrm{i}\theta}}{l}\,\frac{(z-c)\,(z_{\mathrm{t}}-c) - (z-c)\,(z-c+z-z_{\mathrm{t}})\,\mathrm{e}^{2\mathrm{i}\theta}}{2[(z-c)\,(z-z_{\mathrm{t}})]^{\frac{3}{2}}}. \end{aligned}\right\} \tag{B 6}$$

Then the 'consistency conditions' lead to

$$\left.\begin{aligned}\sigma^{\mathrm{P}}_y+\mathrm{i}\tau^{\mathrm{P}}_{xy} &= C^c_1\eta^{\mathrm{R}}+C^c_2\eta^{\mathrm{I}}+[\tau^{\infty}_{xy}+\tau^{\mathrm{P}}_{xy}-\mu(\sigma^{\infty}_y+\sigma^{\mathrm{P}}_y)+\tau_{\mathrm{c}}]\,F^c,\\ \sigma^{\mathrm{P}}_\theta+\mathrm{i}\tau^{\mathrm{P}}_{r\theta} &= C^e_1\eta^{\mathrm{R}}+C^e_2\eta^{\mathrm{I}}+[\tau^{\infty}_{xy}+\tau^{\mathrm{P}}_{xy}-\mu(\sigma^{\infty}_y+\sigma^{\mathrm{P}}_y)+\tau_{\mathrm{c}}]\,F^e,\end{aligned}\right\}\tag{B 7}$$

where

$$\left.\begin{aligned}C^c_j &= \frac{2}{N}\sum_{n=1}^{N}B_j(z^c_{1n},0)+2\sum_{m=2}^{\infty}B_j(z_m,0),\\ C^e_j &= \frac{1}{N}\sum_{n=1}^{N}[B_j(z^r_{1n},\theta)+B_j(z^l_{1n},\theta)]+2\sum_{m=2}^{\infty}B_j(z_m,\theta),\\ F^c &= \frac{2}{N}\sum_{n=1}^{N}S(z^c_{1n},0)+2\sum_{m=2}^{\infty}S(z_m,0),\\ F^e &= \frac{1}{N}\sum_{n=1}^{N}[S(z^r_{1n},\theta)+S(z^l_{1n},\theta)]+2\sum_{m=2}^{\infty}S(z_m,\theta),\end{aligned}\right\}\tag{B 8}$$

with

$$\left.\begin{aligned}z^c_{1n} &= d\,\mathrm{e}^{\mathrm{i}(\phi-\gamma)}-c+2c(n-1)/(N-1),\quad z_m = md\,\mathrm{e}^{\mathrm{i}(\phi-\gamma)},\\ z^r_{1n} &= d\,\mathrm{e}^{\mathrm{i}(\phi-\gamma)}+c+l\,\mathrm{e}^{\mathrm{i}\theta}(n-1)/(N-1),\\ z^l_{1n} &= d\,\mathrm{e}^{\mathrm{i}(\phi-\gamma)}-c-l\,\mathrm{e}^{\mathrm{i}\theta}(n-1)/(N-1).\end{aligned}\right\}\tag{B 9}$$

In (B 7) the first term in the right-hand side of each equation corresponds to the tractions on one particular inhomogeneity, produced because of the presence of the adjacent inhomogeneities, and the second term corresponds to those produced by all other inhomogeneities. The second term in (B 7) can be expanded in even powers of c/md and, in this manner, each series can be summed. In the numerical calculations N is taken to be 10, and terms of an order higher than $(c/d)^{10}$ are neglected.

For given d/c, γ, ϕ, σ_2/σ_1, l/c and θ, the system of algebraic equations (B 2) and (B 6) is solved for η^{R}, η^{I}, σ^{P}_y, τ^{P}_{xy}, $\sigma^{\mathrm{P}}_\theta$ and $\tau^{\mathrm{P}}_{r\theta}$. Then the stress intensity factors at the tips of the extended cracks are obtained from (A 13). The crack orientation angle θ is determined such that the opening-mode stress intensity factor, K_{I}, is maximized. Setting K_{I} equal to the fracture toughness, K_{c}, we obtain the required axial compression, σ_1, for a given crack extension length l/c.

For fixed d/c, γ and ϕ, we calculate the axial compression, σ_1, for each crack extension length, l/c, and for different values of σ_2/σ_1. It turns out that the plot of σ_1 as a function of σ_2 for each l/c is a straight line. From results of this kind we can now calculate various required parameters for a constant confining pressure σ_2, rather than for a constant stress ratio, σ_2/σ_1.

REFERENCES

Ashby, M. F. & Cookley, S. 1986 Fracture from cracks in compression. (In preparation.)

Ashby, M. F. & Verrall, R. A. 1977 Micromechanisms of flow and fracture, and their relevance to the rheology of the upper mantle. *Phil. Trans. R. Soc. Lond.* A **288**, 59–95.

Brace, W. F. & Bombolakis, E. G. 1963 A note on brittle crack growth in compression. *J. geophys. Res.* **68**, 3709–3713.

Donath, F. A., Faill, R. T. & Tobin, D. G. 1971 Deformational mode fields in experimentally deformed rock. *Bull. geol. Soc. Am.* **82**, 1441–1461.

Dugdale, D. S. 1960 Yielding on steel sheets containing slits. *J. Mech. Phys. Solids* **8**, 100–104.

Fairhurst, C. & Cook, N. G. W. 1966 The phenomenon of rock splitting parallel to the direction of maximum compression in the neighbourhood of a surface. In *Proc. 1st Congr. Int. Soc. Rock Mech., Lisbon*, vol. 1, pp. 687–692.

Gerasoulis, A. & Srivastav, R. P. 1981 A method for the numerical solution of singular integral equations with a principal value integral. *Int. J. engng Sci.* **19**, 1293–1298.

Griggs, D. & Handin, J. 1960 Observations on fracture and a hypothesis of earthquakes. In *Rock deformation* (ed. D. Griggs & J. Handin) (*Mem. geol. Soc. Am.* **79**), pp. 347–364.

Hallbauer, D. K., Wagner, H. & Cook, N. G. W. 1973 Some observations concerning the microscopic and mechanical behaviour of quartzite specimens in stiff, triaxial compression tests. *Int. J. Rock Mech. Min. Sci. Geomech. Abstr.* **10**, 713–726.

Hoek, E. & Bieniawski, Z. T. 1965 Brittle fracture propagation in rock under compression. *Int. J. Fract. Mech.* **1**, 137–155.

Holzhausen, G. R. 1978 Sheet structure in rock and some related problems in rock mechanics. Ph.D. thesis, Stanford University, Stanford, California.

Holzhausen, G. R. & Johnson, A. M. 1979 Analyses of longitudinal splitting of uniaxially compressed rock cylinders. *Int. J. Rock Mech. Min. Sci. Geomech. Abstr.* **16**, 163–177.

Horii, H. & Nemat-Nasser, S. 1983 Estimate of stress intensity factors for interacting cracks. In *Advances in aerospace structures, materials and dynamics* (ed. U. Yuceoglu, R. L. Sierakowski & D. A. Glasgow), vol. AD-06, pp. 111–117. New York: ASME.

Horii, H. & Nemat-Nasser, S. 1985*a* Compression-induced microcrack growth in brittle solids: axial splitting and shear failure. *J. geophys. Res.* **90**, 3105–3125.

Horii, H. & Nemat-Nasser, S. 1985*b* Elastic fields of interacting inhomogeneities. *Int. J. Solids Struct.* **21**, 731–745.

Hoshino, K. & Koide, H. 1970 Process of deformation of the sedimentary rocks. In *Proc. 2nd Congr. Int. Soc. Rock Mech., Belgrade*, vol. 1, pp. 353–359.

Kachanov, M. L. 1982 A microcrack model of rock inelasticity, part II: propagation of microcracks. *Mechanics Mater.* **1**, 29–41.

Kirby, S. H. & Kronenberg, A. K. 1984 Deformation of clinopyroxenite: evidence for a transition in flow mechanisms and semibrittle behaviour. *J. geophys. Res.* **89**, 3177–3192.

Kranz, R. L. 1983 Microcracks in rocks: a review. *Tectonophysics* **100**, 449–480.

Lo, K. K. 1978 Analysis of branched cracks. *J. appl. Mech.* **45**, 797–802.

Lockner, D. & Byerlee, J. 1977 Acoustic emission and fault formation in rocks. In *Proc. 1st Conf. on acoustic emission/microseismic activity in geologic structures and materials* (ed. H. R. Hardy, Jr & F. W. Leighton), pp. 99–107. Clausthal-Zellerfeld, Federal Republic of Germany: Trans Tech Publications.

McClintock, F. A. & Walsh, J. B. 1963 Friction on Griffith cracks in rocks under pressure. In *Proc. 4th U.S. Nat. Congr. Appl. Mech. 1962*, vol. 2, pp. 1015–1021. New York: ASME.

Mogi, K. 1966 Pressure dependence of rock strength and transition from brittle fracture to ductile flow. *Bull. Earthq. Res. Inst.* **44**, 215–232.

Murrell, S. A. F. 1965 The effect of triaxial stress systems on the strength of rocks at atmospheric temperatures. *Geophys. Jl R. astr. Soc.* **10**, 231–281.

Muskhelishvili, N. I. 1953 *Some basic problems in the mathematical theory of elasticity*. Groningen, The Netherlands: Noordhoff.

Nemat-Nasser, S. 1983 Non-coplanar crack growth. In *Proc. ICF Int. Symp. on Fract. Mech., Beijing, China, 22–26 Nov.*, pp. 185–197. Beijing, China: Beijing Science Press.

Nemat-Nasser, S. & Horii, H. 1982 Compression-induced nonplanar crack extension with application to splitting, exfoliation, and rockburst. *J. geophys. Res.* **87**, 6805–6821.

Olsson, W. A. & Peng, S. S. 1976 Microcrack nucleation in marble. *Int. J. Rock Mech. Min. Sci. Geomech. Abstr.* **13**, 53–59.

Paterson, M. S. 1978 *Experimental rock deformation – the brittle field*. Springer-Verlag.

Scholz, C. H. 1968 Experimental study of the fracturing process in brittle rock. *J. geophys. Res.* **73**, 1447–1454.

Soga, N., Mizutani, H., Spetzler, H. & Martin, R. J. III 1978 The effect of dilatancy on velocity anisotropy in Westerly granite. *J. geophys. Res.* **83**, 4451–4458.

Sprunt, E. S. & Brace, W. F. 1974 Direct observation of microcavities in crystalline rocks. *Int. J. Rock. Min. Sci. Geomech. Abstr.* **11**, 139–150.

Steif, P. S. 1984 Crack extension under compressive loading. *Engng Fract. Mech.* **20**, 463–473.

Tapponnier, P. & Brace, W. F. 1976 Development of stress-induced microcracks in Westerly granite. *Int. J. Rock Mech. Min. Sci. Geomech. Abstr.* **13**, 103–112.

Tobin, D. G. & Donath, F. A. 1971 Microscopic criteria for defining deformational modes in rock. *Bull. geol. Soc. Am.* **82**, 1463–1476.

Tullis, J. A. 1979 High temperature deformation of rocks and minerals. *Rev. Geophys. Space Phys.* **17**, 1137–1154.

Tullis, J. & Yund, R. A. 1977 Experimental deformation of dry Westerly granite. *J. geophys. Res.* **82**, 5705–5718.

Wawersik, W. R. & Brace, W. F. 1971 Post-failure behavior of a granite and diabase. *Rock Mech.* **3**, 61–85.

Wong, T. F. 1982 Micromechanics of faulting in Westerly granite. *Int. J. Rock Mech. Min. Sci. Geomech. Abstr.* **19**, 49–64.

Wong, T. F. 1985*a* Effects of pressure on micromechanics of faulting in San Marcos gabbro. *J. struct. Geol.* **7**, 737–749.

Wong, T. F. 1985*b* Geometric probability approach to the characterization and analysis of microcracking in rocks. *Mech. Mater.* **4**, 261–276.

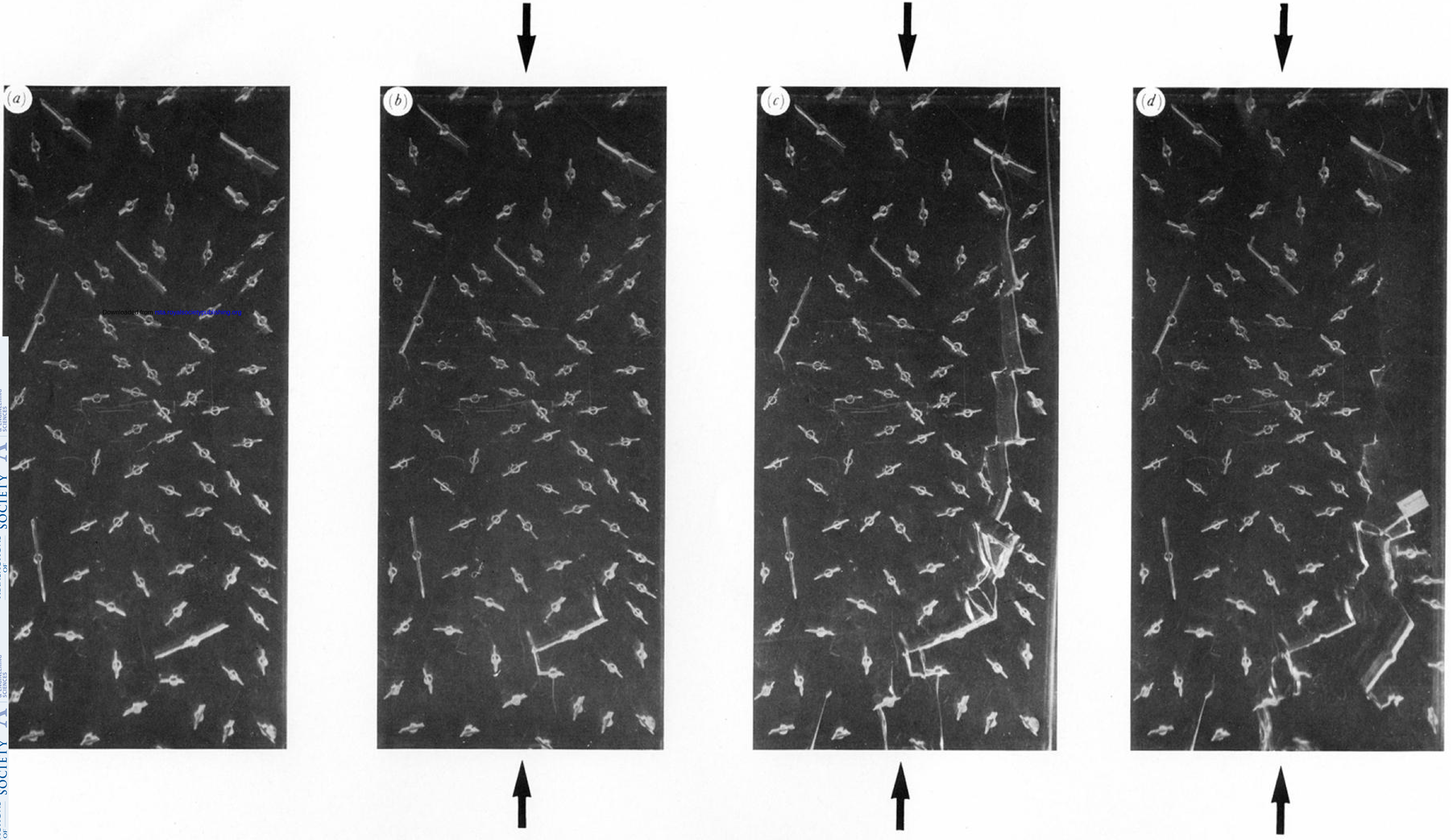

FIGURE 5. (*a*) Specimen containing a large number of flaws. (*b*) Under axial compression *without* confinement, cracks nucleate first at larger flaws; (*c*) axial splitting by the growth and coalescence of cracks; (*d*) shattering of a part of the specimen while many flaws in the remaining part are inactive.

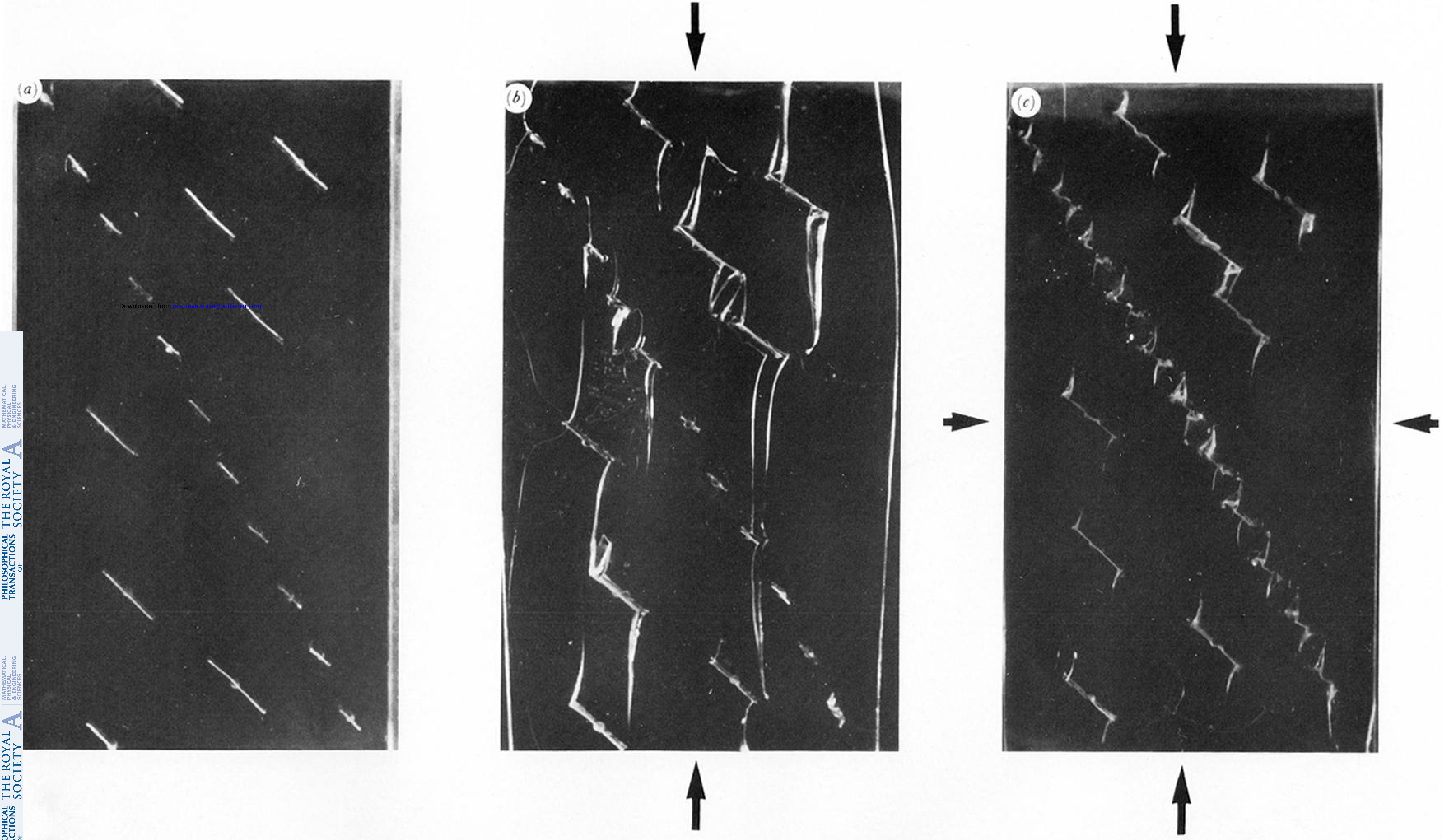

Figure 7. (*a*) Specimen containing a row of small flaws and several larger flaws. (*b*) Axial splitting under axial compression *without* lateral confinement; (*c*) shear failure under axial compression *with* lateral confinement. (From Horii & Nemat-Nasser (1985*a*).)

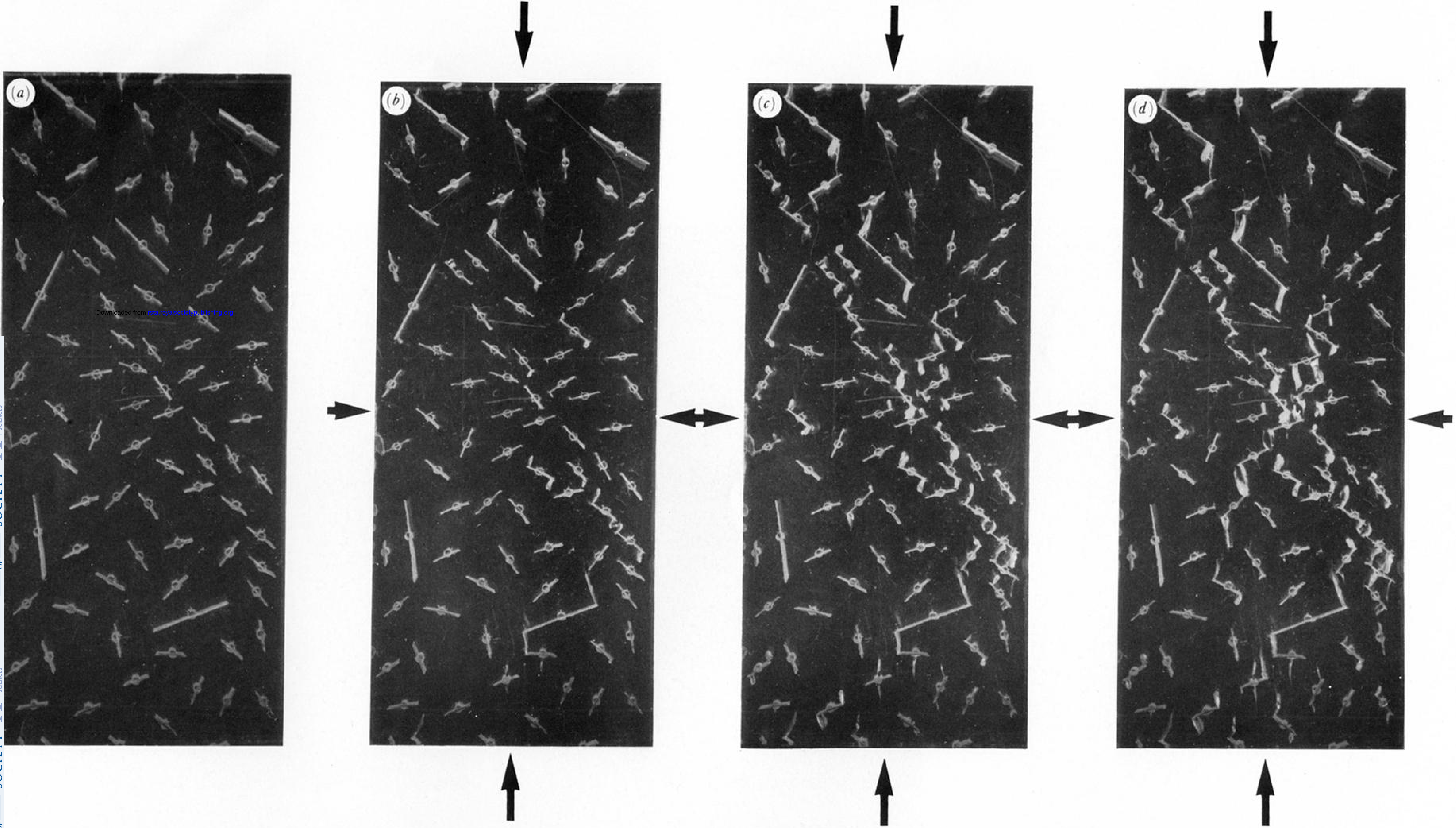

FIGURE 11. (*a*) Specimen containing a large number of flaws. (*b*) Under axial compression *with* lateral pressure $\sigma_2 = 5$ MPa, cracks nucleate at larger flaws: (*c*) cracks at larger flaws are arrested; (*d*) cracks nucleate at smaller flaws, leading to the formation of a fault.

PHILOSOPHICAL TRANSACTIONS OF THE ROYAL SOCIETY A MATHEMATICAL, PHYSICAL & ENGINEERING SCIENCES

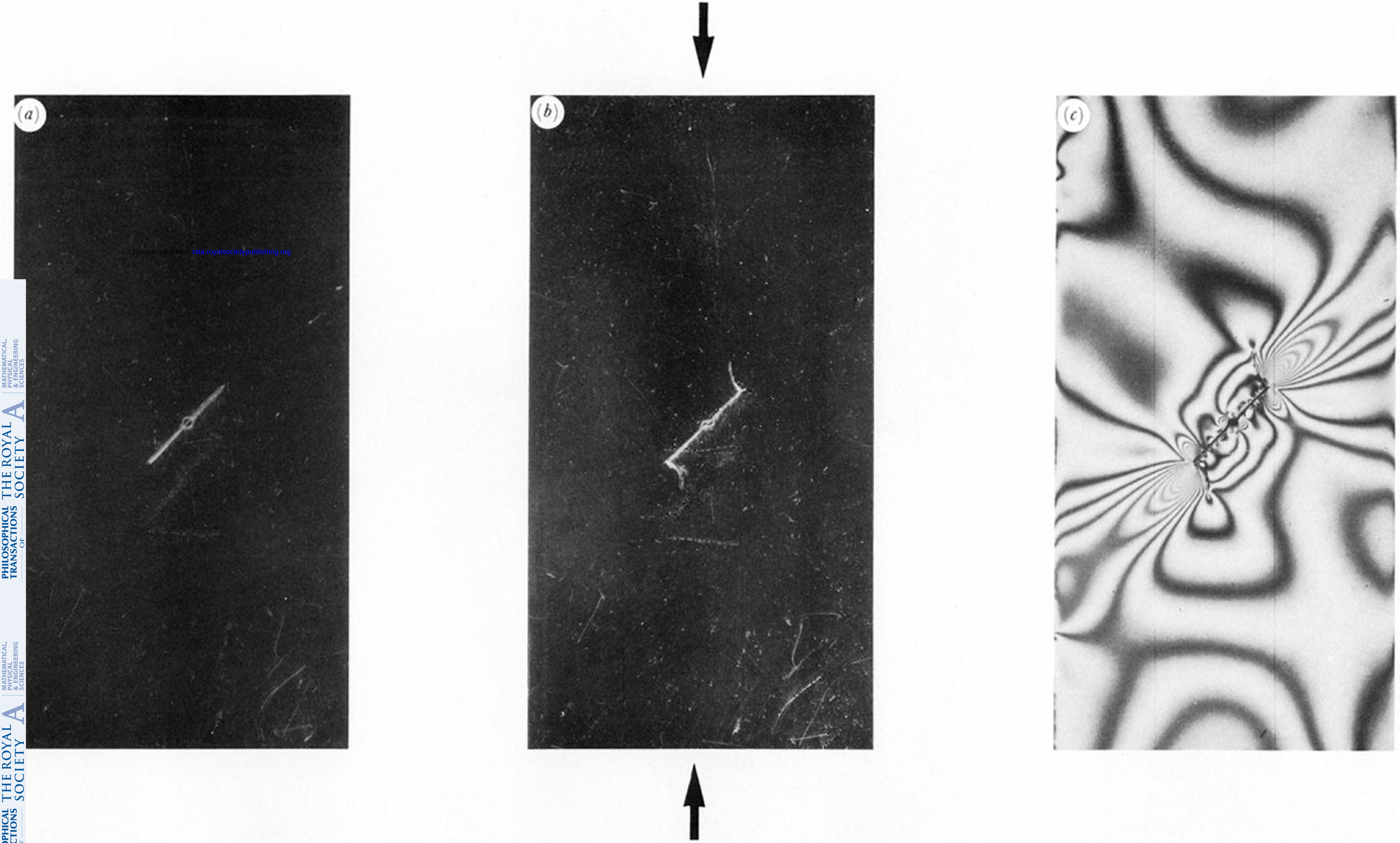

FIGURE 14. (*a*) A specimen with a pre-existing flaw. (*b*) Arrested tension cracks under axial and lateral compressive stresses of constant ratio $\sigma_2/\sigma_1 = 0.05$. (*c*) Photoelastic picture of the unloaded specimen showing the residual strain distribution.

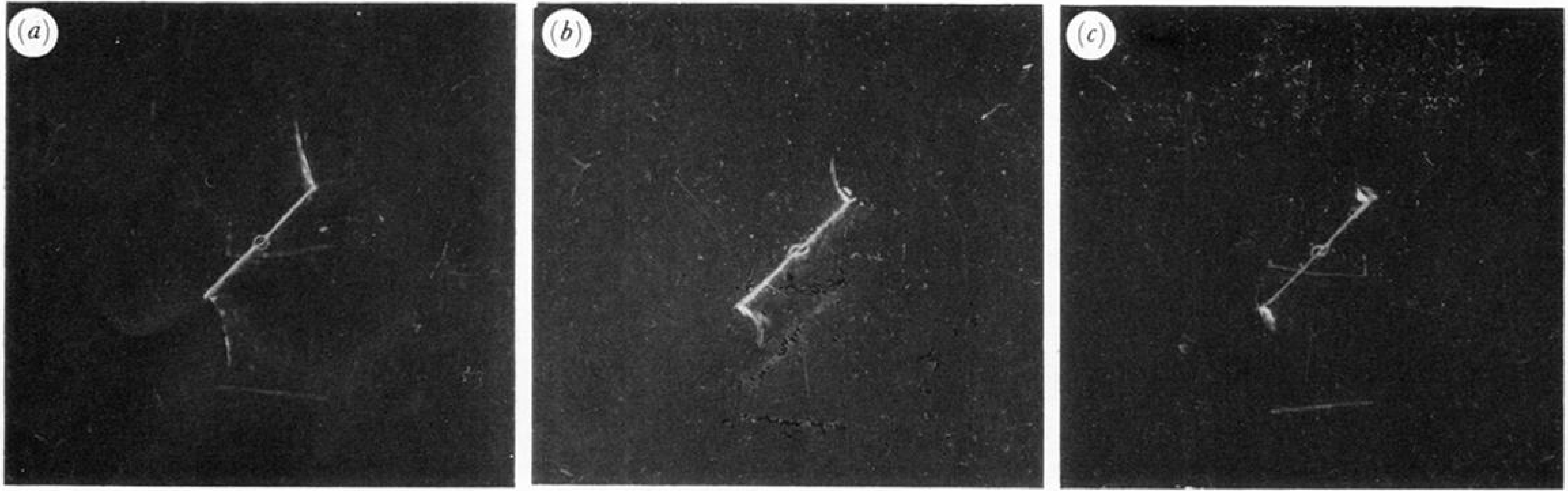

FIGURE 30. Arrested tension cracks emanating from the tips of a 1.8 cm pre-existing flaw for indicated stress ratios, σ_2/σ_1: (*a*) 0.025; (*b*) 0.05; (*c*) 0.1.

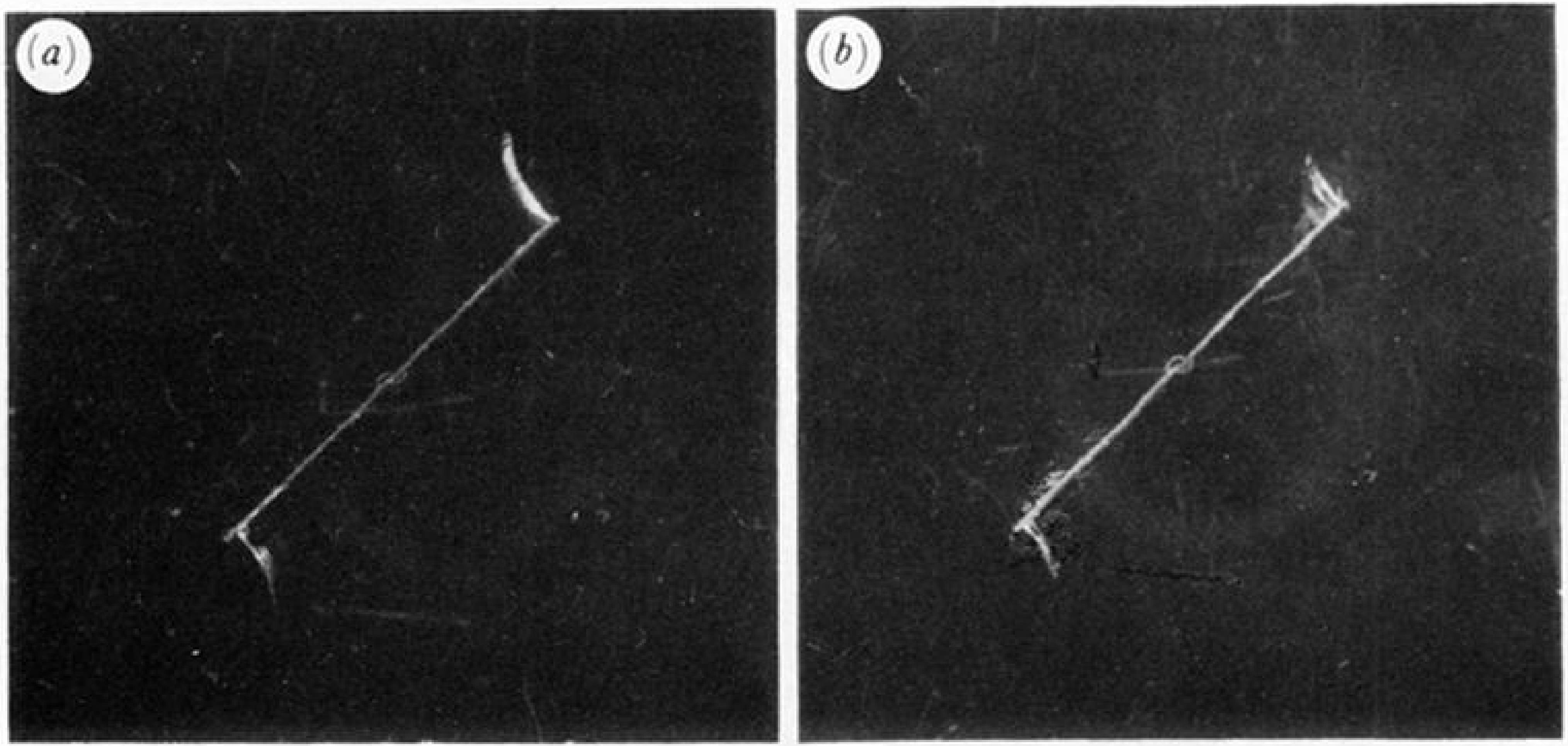

IGURE 31. Arrested tension cracks emanating from the tips of a 3.6 cm pre-existing flaw for indicated stress ratios, σ_2/σ_1: (*a*) 0.1; (*b*) 0.15.

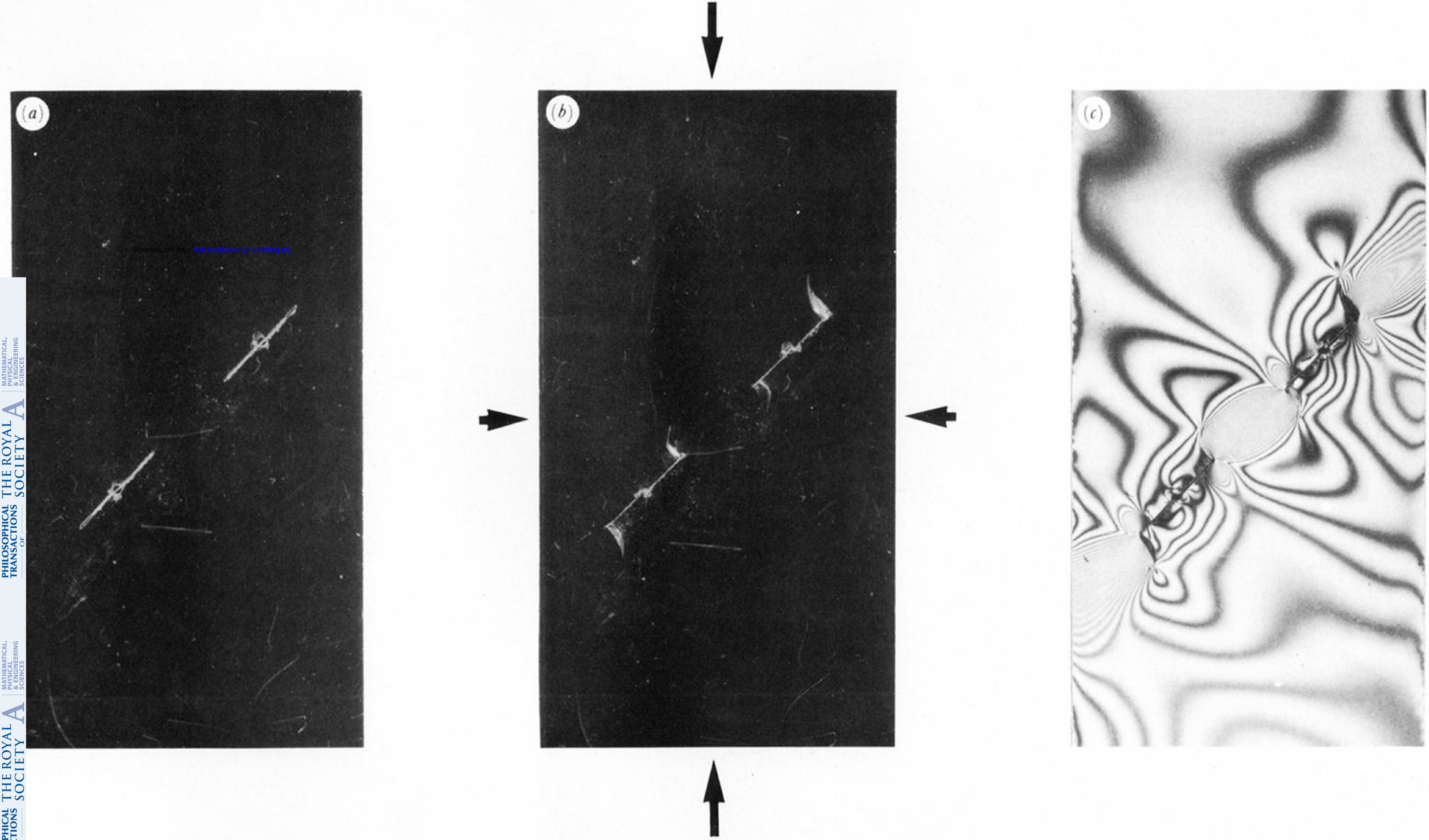

FIGURE 33. (*a*) A specimen with two colinear flaws. (*b*) Arrested tension cracks emanating from the ends of the flaws under axial and lateral compressive stresses of constant ratio $\sigma_2/\sigma_1 = 0.05$. (*c*) Photoelastic picture of the unloaded specimen showing the residual strain distribution.